

1 **Satellites unveil easily-fixable super-emissions in one of the**  
2 **world's largest methane hotspot regions**

3

4 **Authors:** Itziar Irakulis-Loitxate<sup>1\*</sup>, Luis Guanter<sup>1</sup>, Joannes D. Maasakkers<sup>2</sup>, Daniel Zavala-  
5 Araiza<sup>3,4</sup>, Ilse Aben<sup>2</sup>

6

7 **Affiliations:**

8 <sup>1</sup> Research Institute of Water and Environmental Engineering (IIAMA), Universitat Politècnica  
9 de València (UPV), 46022, Valencia, Spain.

10 <sup>2</sup> SRON Netherlands Institute for Space Research, 3584 CA, Utrecht, The Netherlands.

11 <sup>3</sup> Environmental Defense Fund, Reguliersgracht 79, 1017 LN Amsterdam, The Netherlands.

12 <sup>4</sup> Institute for Marine and Atmospheric Research Utrecht, Utrecht University, 3584 CC Utrecht,  
13 The Netherlands.

14

15 \* Correspondence to: iiraloi@doctor.upv.es

16

17 **This paper is a non-peer reviewed preprint submitted to EarthArXiv**

18

19 **Abstract**

20

21 Reduction of fossil fuel-related methane emissions has been identified as an essential means for  
22 climate change mitigation, but emission source identification remains elusive. We combine three  
23 complementary satellite data sets to survey single methane emission sources on the west coast of  
24 Turkmenistan, one of the largest methane hotspots in the world. We found 29 different super-  
25 emitters active in the 2017-2020 time period, 24 of them being inactive flares that are now venting  
26 gas. This suggests a causal relationship between the decrease in flaring and the increase in  
27 venting. At the regional level, 2020 shows a substantial increase in the number of methane plume  
28 detections concerning previous years. Our results reveal that emissions from the west coast of  
29 Turkmenistan could be drastically reduced by proper maintenance of infrastructure and operations,  
30 and that new satellite methods promise a revolution in the detection and monitoring of methane  
31 point emissions worldwide.

32

33 **Introduction**

34

35 Methane (CH<sub>4</sub>) is the second most important anthropogenic greenhouse gas, with a relatively short  
36 lifetime in the atmosphere (9±1 years) and with 86 times the global warming potential of carbon  
37 dioxide over 20 years (1). During the past few decades, CH<sub>4</sub> concentrations have risen rapidly (2)  
38 to record highs that compromise the 2°C temperature target of the Paris Agreement relative to the  
39 pre-industrial era (3). Therefore, the reduction of CH<sub>4</sub> emissions has been identified as a key  
40 climate change mitigation measure in the short to medium term (4).

41

42 Among the sectors with the highest contributions to CH<sub>4</sub> emissions is the oil and gas (O&G)  
43 industry. CH<sub>4</sub> emissions from this sector are particularly difficult to quantify because they are often  
44 the result of unplanned occurrences, i.e. leaks, equipment malfunctions, or abnormal process  
45 conditions, of which quantity, duration, and frequency can differ strongly across regions, operators,  
46 and stages of the O&G supply chain (5). These events can result in so-called super-emissions,  
47 which disproportionately account for a significant fraction of total emissions (6–9). In addition to  
48 unforeseen events, emissions from the sector can come from controlled flaring and venting  
49 processes, which are, respectively, the combustion and direct liberation of excess natural gas  
50 produced. Flaring and venting are primarily done for safety reasons (10), but may also be for  
51 economic or operational reasons (11). The objective of flaring is to avoid the direct release of gas  
52 in the atmosphere by burning it. However, numerous studies show that the use of flaring does not  
53 always guarantee complete combustion of the gas stream in the flare (12–15). Although the use of  
54 flaring is preferable to venting from climate perspective, both are seen as indicators of poor  
55 resource utilization, where the use of more economically and environmentally sustainable  
56 alternatives for the use of excess gas is preferred (16). The use and regulation of flaring and venting  
57 depend on the policies and laws in force in each country or region (16, 17), and only a small number  
58 of geographic areas have been subject to transparent and publicly verifiable reviews of emissions.  
59 Therefore, the credibility of globally reported industrial CH<sub>4</sub> emissions has recently been highly  
60 questioned (5). The IEA (International Energy Agency) Methane Tracker report (18) and the U. N.  
61 report (4) conclude that a large fraction of the emission mitigation options are technically feasible  
62 and cost-effective, and that oil and gas companies can take considerable low-cost and cost-saving  
63 measures to reduce CH<sub>4</sub> emissions from pipelines, drilling and other facilities, but this would require  
64 greater control of all phases of O&G extraction, processing and transport.

65

66 As CH<sub>4</sub> is an odourless and colourless gas for humans, the detection of emissions requires specific  
67 sensors sensitive to the gas. Traditionally, the detection and measurement of emissions have been  
68 performed through onsite campaigns focusing on locations where suspected undeclared emissions  
69 may be present. In situ measurements of ground-based campaigns can be very costly and,  
70 depending on their objective, the data collected will be different. For example, an accurate estimate

71 of emission rates is not necessary for leak detection and repair, whereas for the investigation of  
72 region-wide emission rates the detection of individual sources might not be required. Airborne  
73 campaigns allow coverage of larger areas, but they can be expensive and not very practical in  
74 many cases, like in production fields located in remote places (e.g., in the deserts of the Middle  
75 East) or for the detection of leaks from long-distance pipelines. In this context, satellites are capable  
76 of emission detection and monitoring at different scales (from local to global) and over long periods  
77 of time, as opposed to temporally discrete field measurement campaigns. However, detection from  
78 space will be limited to large emissions.

79 Recently, great advances have been made in the detection and quantification of O&G emissions  
80 from space. Since 2017, the TROPOMI sensor onboard Sentinel-5P provides daily global CH<sub>4</sub>  
81 concentration data with a 7x5.5 km<sup>2</sup> pixel resolution (19). This allows detection of CH<sub>4</sub> concentration  
82 enhancements at the regional scale (e.g., 17–21), but in general, does not enable the determination  
83 of single point sources. On the other hand, the GHGSat instruments and so-called hyperspectral  
84 satellite missions like PRISMA, ZY1 AHSI and Gaofen-5 AHSI are able to map CH<sub>4</sub> plumes from  
85 single emitters at high spatial resolution (25-50 m GHGSat and 30m the rest) with a detection limit  
86 roughly between 100 and 1000 kg/h, suitable to detect medium to strong point emitters worldwide  
87 (13, 25, 26). The systematic application of these measurements, however, is limited by their sparse  
88 spatio-temporal coverage (see Materials and Methods). The recent realisation of the CH<sub>4</sub> mapping  
89 potential of so-called multispectral missions with frequent global coverage holds promise to  
90 alleviate this gap (27). Missions like Sentinel-2 (S2) and Landsat 8 (L8) cover the entire world with  
91 a relatively high spatial and temporal resolution (20 m and less than 5 days revisit time for S2, and  
92 30 m and less than 15 days revisit time for L8), so they are able to continuously monitor CH<sub>4</sub> plumes  
93 under favorable conditions (typically, strong emissions over spatially homogeneous areas). In  
94 particular, S2 provides a very high spatio-temporal sampling and data volume, which makes it to  
95 be the best mission for systematic monitoring of CH<sub>4</sub> sources in those locations where the site  
96 characteristics enable CH<sub>4</sub> retrievals with multispectral missions. L8 and its precursors in the  
97 Landsat series do not provide such a high density of observations but allow to extend the time  
98 series to years and even decades before the S2 era. This recently-developed satellite-based CH<sub>4</sub>  
99 monitoring scenario allows to detect single point emissions of the largest CH<sub>4</sub> hotspot regions in  
100 the world, which are identified with TROPOMI's moderate resolution observations (28).

101 One example of those CH<sub>4</sub> hotspot regions is the west coast of Turkmenistan, located in the Balkan  
102 province on the shores of the Caspian Sea, within the South Caspian Basin (SCB). This is a desert  
103 area where the main human activity is the production of O&G and derived products, with a residual  
104 presence of other possible anthropogenic CH<sub>4</sub> sources such as livestock, rice fields or landfills (29,  
105 30) and an abundant presence of mud volcanoes (more than twenty), some of which are associated  
106 with O&G seepage (31). According to Scarpelli et al. (29), the country of Turkmenistan is one of  
107 the largest emitters of CH<sub>4</sub> from O&G-related sources: eighth in oil-derived emissions (0.88 Tg a<sup>-1</sup>)  
108 and ninth in gas emissions (0.52 Tg a<sup>-1</sup>) in 2016, although the IEA estimates a total of 3.92 Tg a<sup>-1</sup>  
109 of CH<sub>4</sub> emissions in 2020 (almost 3 times more) (18). BP estimates that Turkmenistan has the  
110 fourth-largest natural gas reserves in the world with proven reserves of 19.5 trillion cubic meters,  
111 nearly 10 percent of the world's total, and is in the top 50 largest oil reserves in the world, with  
112 proven reserves of 0.6 thousand million barrels (32). However, its annual production is far below  
113 its potential due to the geopolitical situation it maintains (33). Despite this, short-term forecasts  
114 indicate that production will increase due to an increase in demand from China in the coming years.  
115 Therefore, the country is allocating most of its investments in the energy sector, focusing mainly  
116 on the construction of new pipelines, new phases of exploitation in extraction fields, petrochemical  
117 plants, and compressor stations (33, 34).

118 Within the country, CH<sub>4</sub> emissions are not equally distributed. In recent years TROPOMI has  
119 detected strong CH<sub>4</sub> concentration enhancements in the western coastal belt belonging to the SCB.  
120 In this region there are 26 active fields, 21 onshore and 5 offshore, producing crude oil, condensate,  
121 liquefied natural gas (LNG), and gas in different proportions (see Fig. 1). The SCB is also the only

122 basin producing mainly crude oil in Turkmenistan, in contrast to the other basins, the Kushka and  
123 Amu-Dar'ya Basins (35, 36), which mainly extract gas.

124 In this work, we generate a satellite-based high spatial and temporal resolution survey of CH<sub>4</sub> point  
125 emissions over the west coast of Turkmenistan based on the hotspot locations provided by the  
126 TROPOMI observations. This survey covers an area of approximately 21500 km<sup>2</sup> and the time  
127 period between January 2017 and November 2020. Our analysis relies on three different types of  
128 space-based CH<sub>4</sub> measurements, which are used synergistically: TROPOMI data facilitate the  
129 delimitation of the study area and the identification of the most active regions; the hyperspectral  
130 images from PRISMA and ZY1 AHSI allow the identification of medium-to-strong emitters and the  
131 accurate quantification of emission rates for those regions in a limited set of days; finally, the  
132 multispectral data from S2 and L8 enable the constant monitoring of the emissions from the  
133 emission points unveiled by the hyperspectral data (see Materials and Methods). We choose the  
134 west coast of Turkmenistan for this study because it offers an ideal combination of extreme CH<sub>4</sub>  
135 emissions with a bright and relatively homogeneous surface. This allows us to best evaluate this  
136 unprecedented combination of CH<sub>4</sub> data streams as well as to extract its full potential.

137

138

## 139 **Results**

140

### 141 ***Analysis of emission sources***

142 Combining the hyperspectral and multispectral high spatial resolution satellite data, we have  
143 detected 29 emission points with activity between January 2017 and November 2020 (Fig. 2). The  
144 areas with the highest density of point sources in our high-resolution survey coincide with the  
145 strongest CH<sub>4</sub> enhancements over the west coast of Turkmenistan, as seen in the regional-scale  
146 maps generated from TROPOMI moderate resolution data (Fig. 1)

147 The 20-30 m sampling of the hyperspectral and multispectral satellites in combination with very  
148 high-resolution imagery from Google Earth, Bing Maps and Esri (<2.5m/pix) provide sufficient  
149 information to determine the coordinates of emission sources with high precision, especially for  
150 those emitters with many detected plumes (see Materials and Methods). Combining these data, we  
151 have identified the sources of 26 of the 29 points. We find that the vast majority of the emitters (24  
152 of them) are inactive flares that vent gas. Several of them have flaring activity before 2017  
153 according to the historical record of the S2, Landsat 5, 7, and 8 satellites, and Google Earth, Bing  
154 and Esri images, and three of them had an active flare at the beginning of the study period (Fig.  
155 S1), followed by CH<sub>4</sub> emissions as soon as the flare disappeared. The flaring activity is discussed  
156 in more detail in the following sections.

157 The 24 emitting flares are distributed across different onshore fields of the SCB with a higher  
158 density in the Goturdepe, Barsa-Gelmez and Korpeje fields (Fig. S2, and labeled with emitters A.X,  
159 B.X and D.X, respectively in Fig. 2). These three fields have the highest production (Table 1) and  
160 are also three of the oldest ones in the basin. This coincides with the 2013 Carbon Limits report,  
161 which indicates that most of the flares are concentrated in fields built before 1990 (37). Most of the  
162 emitters are in fields where the predominant activity is crude oil and condensate production, except  
163 for the Korpeje field that extracts mainly gas (see Table 1). Two of the emitting flares are around  
164 an oil power plant linked to the Goturdepepe field. The fields where we have detected emissions  
165 are directly managed by two large state companies, which at the same time control most of the  
166 Turkmenistan fields (35). Although all SCB fields have been analyzed, no emissions have been  
167 recorded between January 2017 and November 2020 from the fields managed by the other five  
168 companies operating in the area, which are based in other countries.

169 Regarding the two other emitters with a known origin, the plumes from points A.10 and E.2 (see  
170 Fig. 2) are due to pipeline leaks that persist over several months. In the case of A.10, the leak is  
171 active for more than a year between 2019 and 2020, while at E.2, we observe emissions from April

172 to October 2018. It has been possible to confirm that these two emissions are due to leaks because  
173 the start of the emission coincides with anomalies in the surface (visible in RGB images), and the  
174 CH<sub>4</sub> plumes seem to originate in pipelines. In E.2, it is also possible to see a liquid spill emanating  
175 from the leak (see Fig. S3).

176 In the case of the three remaining emission points (A.8, A.9 and B.1), it is difficult to attribute them  
177 to a particular source. Leaks are the most likely origin, given that the three points are located just  
178 above pipes, that the facilities are old in these fields and that, according to the 2013 Carbon Limits  
179 report, the pipeline network (controlled by the national gas company Turkmengas) "is characterised  
180 by its old and inefficient equipment" (37). However, we do not have access to records of incidents  
181 or leaks recorded by the operators and cannot confirm the source of the emissions because the  
182 very high-resolution imagery available is not sufficiently up to date to support this hypothesis, and  
183 the resolution of S2 and Landsat imagery is not sufficient in these cases to distinguish a clear  
184 change in the surface in visual imagery. Regarding the temporal evolution of these emissions, point  
185 A.9 only shows emissions during September 2020, which would indicate either that the emission  
186 source has already been fixed or that the emission rates have decreased below the S2 detection  
187 limit. Point A.8 shows emissions since 2017, whereas point B.1 has been emitting at least since  
188 2015, according to L8 detections. Both have maintained emissions at least until the end of our  
189 study period in November 2020.

190 None of the detected emitters is linked to mud volcanoes despite those being potential sources of  
191 CH<sub>4</sub> and having a high presence in the area.

### 192 ***Magnitude of the emissions***

193 We have developed methods to quantify CH<sub>4</sub> concentration enhancements and flux rates from the  
194 hyperspectral data (13). Using the hyperspectral data, we have detected 25 plumes from 12 of the  
195 emitters on different dates (see Materials and Methods). The estimated emission fluxes vary  
196 considerably, with  $1.400 \pm 400$  kg/h being the lowest emission and  $19.600 \pm 8.000$  kg/h the largest  
197 detected emission (see Fig. S4).

198 The coincident overpass time of S2, PRISMA and ZY1 (2 - 5 minutes difference) has enabled us  
199 to capture emissions concurrently with S2 and the hyperspectral systems (see Fig. S5). Using the  
200 accurate CH<sub>4</sub> concentration enhancement maps from the hyperspectral systems as a reference,  
201 we can assess the detection limits of the substantially lower signal-to-noise ratio S2 observations.  
202 This exercise shows that S2 can detect emissions of at least  $1800 \pm 200$  kg/h for the Turkmenistan  
203 desert scenes, as this is the smallest emission for which we have a coincident detection with the  
204 hyperspectral data. This is the minimum flux rate that we set for the plumes detected by S2 (944  
205 plumes in total) between January 2017 and November 2020 (Fig. S4).

206 We have estimated the approximate annual flux emitted from the 29 emitters identified in the study  
207 area, i.e., the total CH<sub>4</sub> flux emitted from the sources that we sample in our study. This calculation  
208 is based on an average flux rate estimated from the 25 plumes detected with the hyperspectral  
209 data and the average emission frequency calculated from the multispectral data set. Further details  
210 of the annual calculation are given in Materials and Methods. As a result, we have obtained a  
211 resulting integrated flux of  $0.28 \text{ Tg a}^{-1}$  ( $0.25\text{-}0.31 \text{ Tg a}^{-1}$  95% confidence interval).

### 212 ***Temporal evolution of the emissions***

213 The monitoring of emissions during 2017-2020 using S2 data has shown a remarkable difference  
214 in the number of detected plumes from each emitter over time. In general, 2018 was the year with  
215 the fewest detected emissions, while 2020 has been the year with the most detected emission  
216 plumes, double the number detected in 2018 (see Fig. 4 and Table 1). This relationship also holds  
217 when we normalize the number of emissions by the number of clear-sky observations in each  
218 period.

219 Not all fields have had the same evolution. Figure 4 shows the examples of the Goturdepe, Korpjeje  
220 and Gogerendag fields (labelled in Fig. 2 with emitters A.X, D.X and C.X, respectively) as  
221 representative cases of different temporal evolution patterns. Goturdepe is one of the fields with  
222 the highest number of identified emitters, and its temporal evolution clearly shows a decrease in  
223 the number of emissions between 2018 and the beginning of 2019, while in the years 2017 and  
224 2020, the emission density is notably higher. Regarding the Korpjeje field, Varon et al. reported in  
225 2019 emissions from three different points (25), one of which is named in this paper as D.7.  
226 Immediately after the article submission (May 2019) emissions stopped from that source, but both  
227 our analysis and the one by Varon et al. (2021) (27) show that emissions resumed after a few  
228 months (according to our observations in September 2019, see Fig. S6 emitter D.7). Finally, the  
229 Gogerendag field stands out for the direct relationship between the end of the use of flaring and  
230 the start of emissions, i.e., at the beginning of the monitoring period, emitters in this field had flaring  
231 activity, but CH<sub>4</sub> emission events began to occur right after the flaring signal was no longer visible.  
232 In the second half of 2019, it can be seen how after several months of flaring inactivity, both emitters  
233 released CH<sub>4</sub> on the same day, and then a flare is observed intermittently at C.1 before it remains  
234 off at least until the end of our study period. Once flaring was inactive, the number of CH<sub>4</sub> emissions  
235 detected by S2 increased. This same flaring-emission relationship is repeated at point F.3, which  
236 shows an intense flaring signal at the beginning of the study, but in July 2018, the flaring  
237 disappears. In July 2019, CH<sub>4</sub> emissions start to be observed intermittently until the end of the  
238 study period (Fig. S6 emitter F.3).

239 Analysing the emitters individually, we also see that there is wide variability in their emitting  
240 frequency. Of the 29 points, 6 show emissions on only between 1 and 3% of the observed clear-  
241 sky days, i.e., they rarely present emissions above our 1800 kg/h detection limit. On the opposite  
242 side, 5 points show emissions in more than 38% of the observed days. For example, Figure 3  
243 shows a S2 detection series from A.3 (29% emission frequency) whose emissions persist during  
244 the entire 2017-2020 period. The low frequencies imply that we have detected large CH<sub>4</sub> emissions  
245 between 1 and 7 times during the whole observation period, these emissions could be explained  
246 by emergencies or well purging, that are very unusual events, and where the law allows the venting  
247 of large amounts of gas from flaring systems for a short period. However, the more frequent emitters  
248 would conflict with the "Rules for the Development of Hydrocarbon Fields" of the Turkmen law,  
249 which bans continuous gas flaring and venting (37). Detailed information on the frequency of  
250 emissions is provided in Table S1 and Figure 2, and the temporal evolution of each emitter in Fig.  
251 S6.

252 We also look at the emissions of the region before our 2017-2020 core study period. First, the  
253 longer time series of L8 satellite data reveal that at least 15 of the 29 emitters identified in the study  
254 period were already emitting large amounts of CH<sub>4</sub> before January 2017, as shown in Figure 3 (first  
255 window, right-hand side panel) and Fig. S7. Second, the SCIAMACHY sensor onboard ENVISAT  
256 (38) also provides information on the history of emissions in the area, in this case, at the regional  
257 scale. Comparing the distribution of our single detections with the regional XCH<sub>4</sub> map from  
258 TROPOMI (Figs. 1-2), we can infer that the CH<sub>4</sub> enhancement observed by TROPOMI in the  
259 northern part of the study area is the result of many moderate to high-frequency emitters, while in  
260 the south the areas of CH<sub>4</sub> enhancement are related to one or a few very high-frequency emitters  
261 (Fig. S8). This relationship holds in older data from SCIAMACHY. Between 2003-2010  
262 SCIAMACHY already observed a higher CH<sub>4</sub> concentration in the northern area of the SCB, over  
263 the Goturdepe and Barsa-Gelmez fields (emitters A.X and B.X) and another hot spot over the  
264 Korpjeje (D.X) and Gamyshlja Gunorta (E.X) fields but did not observe a CH<sub>4</sub> enhancement over  
265 the southernmost Keymir (F.X) and Akpatlavuk (G.X) fields. If we look at the year of installation of  
266 the facility, we find that most of the emitters in the first four fields already existed before 2010, but  
267 emitter F.1, which is the one with the highest frequency in Keymir, was built just in 2010, according  
268 to Landsat images, and emitter G.1, the only one in Akpatlavuk, was built in 2015. So, these two  
269 points did not contribute to the average result of the data collected by SCIAMACHY (Fig. S8). On

270 the other hand, emitters F.1 and G.1 did not exist during that time, and thus their emissions are  
271 only reflected in the TROPOMI data set.

272 Occasional lookups of Landsat 5 (L5) historical data reveal that emissions have been present in  
273 these fields since, at least, 1987. Figure 5 shows emissions from three active sources in the past,  
274 other than those identified between 2017-2020. The first (P.1) is located about 200 m from source  
275 A.6 and records emissions from 1987 to, at least, 1999 very frequently. Two years after the last  
276 observed emission from P.1, the P.2 emitter, about 350 m north of A.6, began emitting continuously  
277 from June through, at least, September 2001. Finally, the third source (P.3) is 1.15 km from emitter  
278 A.4, and we have only identified one emission in the Landsat searches. As we do not have very  
279 high-resolution data for these dates, nor detailed information about the infrastructure, we have not  
280 attributed these emissions to any specific infrastructure.

281 All these data demonstrate that this type of emission has been occurring for many years and that  
282 the origin of these long-term CH<sub>4</sub> enhancements is in the venting of gas, mainly from oil and  
283 condensate fields.

## 284 ***Flaring***

285 According to VIIRS data, flaring has been progressively decreasing over the SCB since 2016. For  
286 example, the flare volume in 2019 was about 40% lower than in 2012 (Fig. S9). This trend is the  
287 same if we look at the state-level data, where the flare volume has continuously decreased since  
288 VIIRS records have been kept, and in 2019 it is almost half of what it was in 2012 (2.42 billion cubic  
289 meters in 2012 and 1.34 billion cubic meters in 2019) (39).

290 As we previously discussed, several of the CH<sub>4</sub> emitters detected in our survey follow this trend of  
291 flaring reduction. In particular, C.1, C.2 and F.3 have flaring activity at the beginning of the  
292 monitoring but then change from flaring to gas emission. In addition, we have observed that at least  
293 six other emitters had an active flame in the past, but vented gas later (Fig. S1). The fact that  
294 several of the emitters currently venting CH<sub>4</sub> showed flaring activity in the past suggests a  
295 relationship between the decrease in flaring at the expense of an increase of venting.

296 The effect of the use of flaring can also be noticed in the TROPOMI data where, for example, we  
297 see the influence of point E.1 (high-frequency emitter of the Gamyshlja-Gunorta field). This emitter  
298 kept showing flaring activity until 2005 while it is emitting CH<sub>4</sub> during the TROPOMI monitoring  
299 period. On the other hand, we hardly see the influence of the two Gogerendag emitters (C.1 and  
300 C.2), which kept the flare active until 2019, and their emissions are still not noticeable in the  
301 TROPOMI data (Fig. S8).

302

## 303 **Discussion**

304

305 In this study, we have used a combination of satellites to produce a large-scale survey of individual  
306 CH<sub>4</sub> emitters active between 2017 and 2020 on the west coast of Turkmenistan, one of the world's  
307 largest CH<sub>4</sub> hotspot regions as shown by TROPOMI observations. First, areas of interest within the  
308 region have been identified using medium-resolution data from TROPOMI. Two types of high-  
309 resolution data (multi- and hyperspectral) have then been used to detect, quantify, and monitor the  
310 activity of the identified 29 strong CH<sub>4</sub> emitters over time. In particular, hyperspectral satellites have  
311 mapped plumes with fluxes between  $1.400 \pm 400$  kg/h and  $19.600 \pm 8.100$  kg/h, which indicates  
312 that the emissions from Turkmenistan are often extremely high; the S2 multispectral satellite has  
313 enabled the systematic monitoring of emissions above 1800 kg/h, showing an increase in the  
314 number of detections in 2020 compared to the previous years, and the longer time series of the L5  
315 and L8 missions (1984-2012 and 2013-today respectively) has shown that several emitters have  
316 been venting CH<sub>4</sub> beyond the S2 observation period.

317

318 The main results of this study reveal that the large amounts of CH<sub>4</sub> emitted in this region are mainly  
319 due to the venting of gas from oil fields. We find that venting is related to the decrease in the use  
320 of flaring as a method to treat excess gas. Secondly, the emissions not related to venting are linked  
321 to the bad condition of the installations, concretely of the pipelines, which have gas leaks during  
322 long time periods. These emissions could be easily and rapidly fixed: in the case of inactive flares  
323 it would be sufficient to activate the flares, although other more sustainable methods as gas capture  
324 would be preferable (40); in the case of pipeline leaks, it is necessary to improve maintenance and  
325 surveillance. Identifying these high emitting sources is fundamental for any mitigation strategy, as  
326 their elimination would result in an important reduction of CH<sub>4</sub> emissions. In particular, we estimate  
327 that the emissions identified in this study amount to 0.28 Tg a<sup>-1</sup> (0.25-0.31 Tg a<sup>-1</sup> 95% confidence  
328 interval), which could be easily avoided. It is unknown how these numbers would scale to the global  
329 scale, but we can already speculate that a massive amount of CH<sub>4</sub> emissions could indeed be  
330 avoided if greater control actions were taken on oil and gas extraction operations.

331  
332 The emitting sources found in the study only represent emitters above the detection limit of the  
333 satellites used in this work. In these cases, synergy with a regional mapper (and inverse modelling)  
334 such as TROPOMI or the upcoming MethanSAT missions could provide the full picture of emissions  
335 for the basin. In addition, rapid source identification and data interpretation can provide valuable  
336 clues to understand the problem in each case, and thus select appropriate methods for effective  
337 mitigation of smaller emissions.

338  
339 High-resolution satellites capable of detecting CH<sub>4</sub> emissions, in combination with mid-resolution  
340 satellites with daily global coverage such as TROPOMI and its successor Sentinel-5 instruments,  
341 bring a new era in the monitoring of industrial emissions, both locally and globally, with the potential  
342 to provide early warnings in near real-time. In addition to the already operational high-resolution  
343 satellites (GHGSat, PRISMA, ZY1, S2 and Landsat), new missions such as MethaneSAT, EMIT,  
344 Carbon Mapper, EnMAP, CHIME or SBG are expected to reinforce possible monitoring systems  
345 even further.

346  
347 Our results also point to the risks of penalizing flaring without effective measures to control venting.  
348 The possibility of flaring cessation at the expense of venting is a problem that has been discussed  
349 in the past (40) since monitoring flaring is easy to carry out by satellites, but venting was easy to  
350 hide until now. Furthermore, the methods we use here can also be applied to track the progress of  
351 flare reduction strategies in other areas of the world.

352  
353

## 354 **Materials and Methods**

355  
356  
357

### 356 ***Definition of the study area with TROPOMI XCH<sub>4</sub> data***

358 The TROPospheric Monitoring Instrument (TROPOMI) sensor onboard ESA's Sentinel-5P satellite  
359 (19) provides daily global coverage of CH<sub>4</sub> data with 7 km x 7 km (since August 2019 5.5 km x 7  
360 km) pixel resolution in nadir that allows finding areas with high CH<sub>4</sub> concentration enhancements.  
361 The approximate location of the strongest sources in the study area has been identified using the  
362 wind rotation method introduced by Maasackers et al. (2021) (28). After identification of an area  
363 with large CH<sub>4</sub> concentrations, data from individual days is rotated around a possible target point  
364 using the wind direction at the location. In this manner, the scenes are rotated so that the wind  
365 vector is always pointing northward, these rotated scenes are then averaged. By doing these  
366 exercises for a full grid of points, the location can be determined where the mean downwind  
367 concentrations are most significantly enhanced compared to the mean upwind concentrations,  
368 resulting in the most likely location of the source (28). TROPOMI pinpointing identified five key  
369 points (see Fig. S10) where we started the search for point sources of emission. In addition, the  
370 Korpeje area was already known for its strong and frequent point source emissions (25).

371

372 ***High-resolution Hyperspectral & Multispectral data***

373

374 This study has used both hyperspectral and multispectral satellites, which are complementary for  
375 the detection and monitoring of CH<sub>4</sub> emissions. Hyperspectral instruments offer a relatively high  
376 sensitivity to CH<sub>4</sub> thanks to tens of spectral channels located around the strong CH<sub>4</sub> absorption  
377 feature around 2300 nm, but acquisitions are made upon request and their coverage is sparse in  
378 space and time. In turn, multispectral systems provide frequent and spatially-continuous  
379 observations over any region on Earth, but with very limited sensitivity to CH<sub>4</sub>.

380

381 *Use of hyperspectral data for CH<sub>4</sub> detection and quantification*

382

383 For this study, we have collected data from the ZY1 AHSI and PRISMA missions, which are the  
384 only two hyperspectral satellite missions sampling the 2300 nm spectral region and with an open  
385 data policy. The Chinese ZY1 mission was launched in September 2019 and has onboard the AHSI  
386 sensor whose images cover a 60X60 km<sup>2</sup> area, while the Italian PRISMA mission, launched in  
387 March 2019, provides images with 30X30 km<sup>2</sup> coverage. Both missions have a spatial resolution  
388 of 30 m.

389

390 All hyperspectral data acquisitions took place during 2020 (the last year covered by this study).  
391 Acquisition requests were first made with a focus on the key points identified by TROPOMI, and  
392 then those were extended to other possible key areas (see the following subsection). Due to the  
393 difficulty to obtain data from these sensors in the short term, we could not cover some areas in that  
394 time range. Many PRISMA images have been acquired from the catalogue, while others have been  
395 obtained based on requests for targeted locations. In total, we have obtained 12 images from  
396 PRISMA and one from ZY1 (see Fig. S11).

397

398 The hyperspectral images have allowed us to observe CH<sub>4</sub> emissions with 30m spatial resolution  
399 and quantify the emissions using the matched filter method (13). The quantification has been done  
400 with the integrated mass enhancement (IME) method (41), and we have used 1-h average 10-m  
401 wind (*U*10) data from the NASA Goddard Earth Observing System-Fast Processing (GEOS-FP)  
402 meteorological reanalysis product at 0.25°x 0.3125° resolution (42) to get the Flux Rates (*Q*). The  
403 details of our processing of hyperspectral data are provided in Guanter et al. (2021) (43).

404

405 *Use of multispectral data for CH<sub>4</sub> monitoring*

406

407 For the temporal monitoring of emissions, we have used the Sentinel-2 Level 2A (L2A) product  
408 from both S2-A and B satellites of ESA's Copernicus program, whose data are openly available on  
409 the Copernicus Open Access Hub official portal.

410

411 The S2 CH<sub>4</sub> detection limit and the estimation of the emissions detected in S2 monitoring has been  
412 defined using the quantified plumes coincident with S2 detections, as the three satellites have  
413 approximately the same overpass time with a few minutes difference (between 2 and 5) in the  
414 observations used. We have identified nine simultaneous plumes indicating that the detection limit  
415 of S2 is close to 1800 kg/h (see Fig. S5). This relationship holds if the plume maintains  
416 concentrations above ~3800 ppm m. For example, in cases where the wind speed is very high, and  
417 the emitted gas disperses rapidly, the plume tail disappears, and the pixels in the plume have lower  
418 concentrations despite being associated with a high emission flux. There are several examples of  
419 this in Figure S4, where hyperspectral sensors detect plumes on 2020-07-31 and 2020-09-11 that  
420 S2 missed, i.e., S2 has not detected emissions with fluxes lower than 1800 kg/h that PRISMA and  
421 ZY1 have with a few minutes difference. This detection limit value is slightly lower than Varon et al.  
422 (2021) (27) indicated (~3000 kg/h) for the most optimal surfaces, as is the case in most of  
423 Turkmenistan.

424

425 The detection of single plumes from S2 data is often challenging because of its relatively low  
426 sensitivity to CH<sub>4</sub> concentration enhancements. We have a priori predetermined areas with potential  
427 emitters on which to focus the search of possible plumes. These are: the area near the TROPOMI  
428 pinpoints (see Fig. S10), emission points detected in the ZY1 and PRISMA hyperspectral images  
429 (see Fig. S4), O&G extraction fields in the SCB according to (35, 36), pipeline crossings, flares that  
430 in the past had shown an active flame, and mud volcanoes.

431  
432 To detect CH<sub>4</sub> emissions with S2, we have selected bands B11 and B12, with 20 m pixel resolution.  
433 The B11 band extends over a set of weak CH<sub>4</sub> absorption lines near 1650 nm, and the B12 band  
434 includes stronger absorption lines in the 2200-2300 nm range so that the average optical depth of  
435 CH<sub>4</sub> in B12 is five times that of B11 (27). The identification of emissions has been carried out using  
436 a dynamic multitemporal method, where we consider all observed days by both the S2 A and B  
437 satellites. We have applied the B12/B11 band ratio to the clear-sky days and, using the timelapse  
438 tool provided in the online service EO Browser of Sentinel Hub (44), we have obtained the  
439 continuous record of the time series of the study area (<3 km<sup>2</sup> in each timelapse). We have  
440 discarded cloudy images with an automatic filter available in the EO Browser service and manually  
441 sandstorm days that do not allow a clear view of the surface.

442  
443 The S2 detection figures shown in this paper (Fig. 3 and Fig. S5) have been obtained applying the  
444 B12 and B11 bands ratio of two contiguous days from the same satellite and with the same orbit  
445 whenever possible, i.e., the equation described below but ensuring that the detection is taken by  
446 the same satellite, S2A or S2B from the same viewing, on both days. In this way, we try to avoid  
447 the increase of noise in the result due to miss-registration and viewing differences (45).

448

449

$$R = \frac{B12/B12'}{B11/B11'}$$

450

451

452 where  $R$  is the result of the band ratio  $B12$  and  $B11$  are the bands of the emission day, and  $B12'$   
453 and  $B11'$  are the bands of the nearest clear-sky day observed with the same S2A or S2B satellite  
454 on which there is no emission. This method provides the CH<sub>4</sub> plume avoiding the maximum  
455 interference in the signal from other surface components.

456

457 The simple B12/B11 band ratios provide an image where CH<sub>4</sub> pixels take low values (<0.9) which  
458 contrast with the rest of the surface that is close to 1. The result would be similar to the one  
459 proposed by Varon et al. (2021) (27) in the Multi-Band/Single-Pass (MBSP) method, but in this  
460 case, without normalising the band ratio and dynamically comparing the emission days with the  
461 adjacent days. The comparison of each image with the days immediately adjacent to it using the  
462 timelapse allows enhancing the CH<sub>4</sub> signal by minimizing the effect of surface variability since the  
463 CH<sub>4</sub> plumes change shape depending on the activity, emission intensity of each day, and the wind  
464 direction that normally changes from one day to another. This dynamic method has proven to be  
465 the most effective to identify the weakest emissions, which, analysed individually, would go  
466 unnoticed, and to lower the detection limit of S2 to about 1800 kg/h on the most optimal surfaces.  
467 The 20m pixel resolution of S2 and multiple observations of plumes from the same source have  
468 provided sufficient accuracy to identify the emission source.

469

470 We have obtained the results for L5 and L8 in the same way as S2, but in this case, the bands  
471 extending over the weak CH<sub>4</sub> absorption lines are B05 in the case of L5 (1550-1750 nm) and B06  
472 in the case of L8 (1570-1670 nm), and B07 covers the strong absorption lines in both cases (2080-  
473 2350 nm in L5 and 2110-2290 nm in L8) with a 30 m resolution. In the case of L8, the overpass  
474 time is about 20 minutes different from ZY1, PRISMA and S2, so that coincident detections on the  
475 same day have not been considered valid for empirical comparison. We have used the data from  
476 the entire L5 time series (1984-2012) to observe specific locations with high emission potential,

477 and the L8 time series (2013-present) to observe all locations of emitters identified with S2. Both  
478 satellites have a revisit cycle of 16 days (46).

479

### 480 **Annual quantification**

481

482 We have estimated an integrated annual emission rate ( $Q_a$ ) from all 29 sources detected in this  
483 study with S2. For this estimation, we rely on the  $Q$  values estimated for the single plumes obtained  
484 from the hyperspectral data (Fig. S4) in order to obtain an average hourly flux rate ( $\bar{Q}$ )  
485 characterizing the emissions in the area. This average flux rate is scaled in time using an average  
486 emission frequency number ( $\bar{f}$ ) which is obtained from the S2 plume detections (O. E. % in Table  
487 S1). The total annual emission rate is then given by:

488

489

$$490 Q_a = 24 \cdot 365 \cdot N \cdot \bar{Q} \cdot \bar{f}$$

491

492

493 where  $N$  is the number of emitters, i.e., 29 emission sources.

494

495 This estimate is based on statistics from emission intensity and frequency data sampling the four  
496 years of monitoring covered in this study. The resulting annual flux only represents the annual  
497 emission flux from large emitters, and underestimates the real one, as only emissions above the  
498 S2 detection limit are considered in the calculation of the average emission frequency. As a result,  
499 we have obtained an annual estimate of 0.28 Tg of CH<sub>4</sub> emitted per year, with a 95% confidence  
500 interval between 0.25 and 0.31 Tg a<sup>-1</sup>.

501

502 The 95% confidence interval was obtained by non-parametric bootstrapping of all the results  
503 obtained from combining the  $Q$  of each of the 25 plumes with the emission frequencies ( $f$ ) of each  
504 of the 29 identified emitters.

505

### 506 **Emitter identification**

507

508 The identification of the sources was carried out by inspection of high-resolution visual images from  
509 Google Earth, Bing Maps and Esri, depending on the acquisition date available for each area on  
510 each platform.

511 In the initial approach of the study, we also considered mud volcanoes as possible sources of CH<sub>4</sub>  
512 emission. However, after observing the different potential areas, it has not been possible to link any  
513 of the observed plumes to a mud volcano.

514 In three cases, we were not able to identify the origin of the emissions due to lack of up-to-date  
515 very high-resolution surface imagery (in some southern areas most recent image is from 2015 and  
516 Planet's 3m/pix images are not enough for these cases) and insufficient geographic information  
517 about Turkmenistan's O&G infrastructure.

518 Regarding the emitters identified as flares, there is a wide variety of flare systems within the O&G  
519 sector of which characteristics depend on multiple factors such as calorific power of the burning  
520 fuel, physical state (gas, liquid, or mixture), pressure, flow, geographic location for the population  
521 or other activities, availability of land for the installations, economic availability, ... In general, we  
522 can distinguish two main groups of flares: elevated flares that are mainly used in the burning of  
523 gaseous waste in plant emergencies (due to power failures, composition, and fires) and are more  
524 oriented to sudden alterations, and ground flares that are generally used for moderate or  
525 continuous flow. Linked to the second, we can distinguish a third group, the pit flares, which usually  
526 burn liquid or gaseous waste in unpopulated areas to meet environmental standards.

527 In Turkmenistan, we have detected emissions from all three types of flares. Throughout the study,  
528 they have all been referred to as the same "flare" emitter type, although in Table S1, there is a  
529 more precise classification separating them into the three groups.

530 The identification of the emitters, mainly flares, has been verified by the Carbon Limits group, which  
531 has experience in field measurements in Turkmenistan.

532

### 533 ***Flaring signal***

534

535 Flaring can be detected by satellites with bands in the SWIR, due to the flame's strong signal in  
536 that spectral region, with the emission peak at 1.6  $\mu\text{m}$  (47).

537

538 In the 2017-2020 period, three of the emission points have shown an intense signal in the B12  
539 band of S2 coming from flaring, i.e., those days the excess gas was burning instead of venting it  
540 directly to the atmosphere. These three points maintained a constant signal for several months until  
541 the flaring signal disappeared, and we started detecting CH<sub>4</sub> emissions (see Fig. 4 Gogerendag  
542 case). S2 data are only available as of January 2017, so to check if there had been any flaring  
543 signal in the past for the rest of the emitters, we have observed with Landsat 8, 7 and 5 data (up to  
544 1984) (48), using the Google Earth Engine platform, the historical VIIRS signal (up to 2012) using  
545 SkyTruth's flaring maps (39, 49), and FIRMS for MODIS (up to 2000) and additional information  
546 from VIIRS. We have also used historical high-resolution Google, Bing and Esri imagery to check  
547 if flaring was also used in the past, as the powerful flaring flames can also be seen in the visible  
548 (see Fig. S1).

549

### 550 **Acknowledgments**

551

552 The authors thank the team that realized the TROPOMI instrument and its data products, consisting  
553 of the partnership between Airbus Defense and Space Netherlands, KNMI, SRON, and TNO,  
554 commissioned by NSO and ESA. Sentinel-5 Precursor is part of the EU Copernicus program,  
555 Copernicus (modified) Sentinel-5P data (2018-2020) have been used. We thank the Sentinel Hub  
556 service for providing the EO Browser service, which was key to the development of the study.  
557 Thanks to the Environmental Defense Fund (EDF) for providing data about the O&G fields of the  
558 study area, and the Carbon Limits group for contributing to the verification of the emission sources.  
559 We thank the Italian Space Agency for the PRISMA data used in this work. Dr. Yongguang Zhang  
560 from the University of Nanjing is also thanked for his support to get access to ZY1 AHSI data, and  
561 Dr. Javier Gorroño from Universitat Politècnica de València for his assistance in the uncertainty  
562 estimations.

563

564

## References

565

566

567

568

569

570

571

572

573

574

575

576

577

578

579

580

581

582

583

584

585

586

587

588

589

590

591

592

593

594

595

596

597

598

599

600

601

602

603

604

605

606

607

608

609

610

611

612

613

614

615

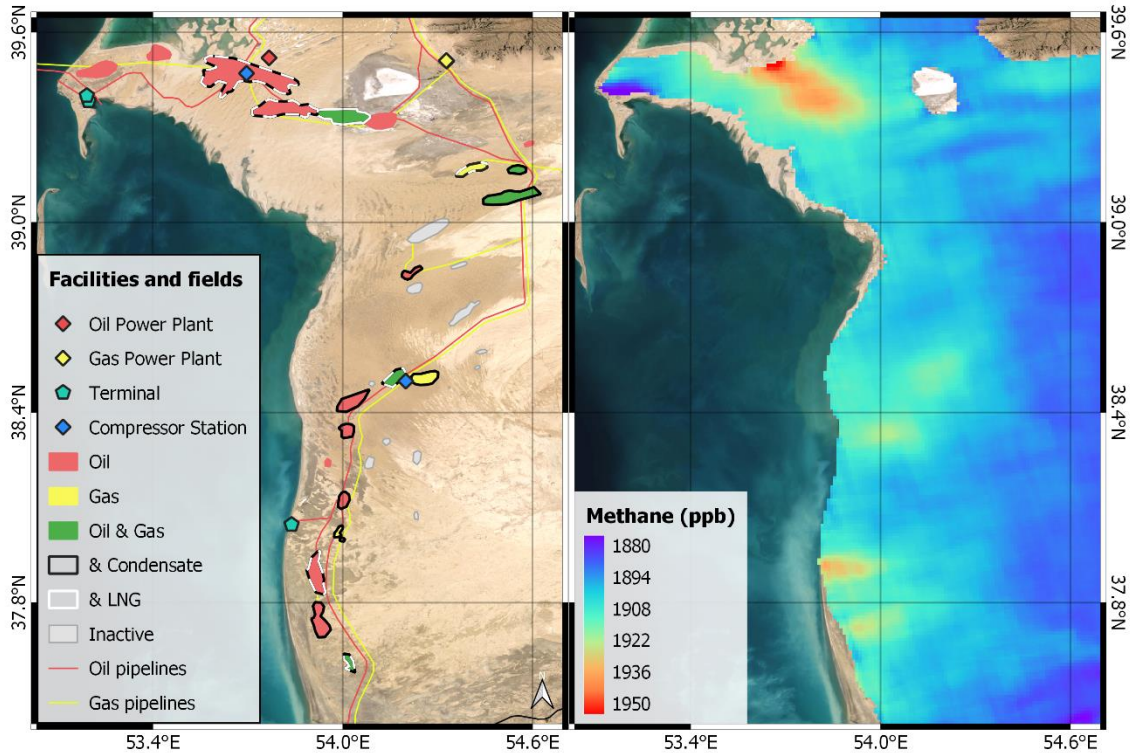
616

617

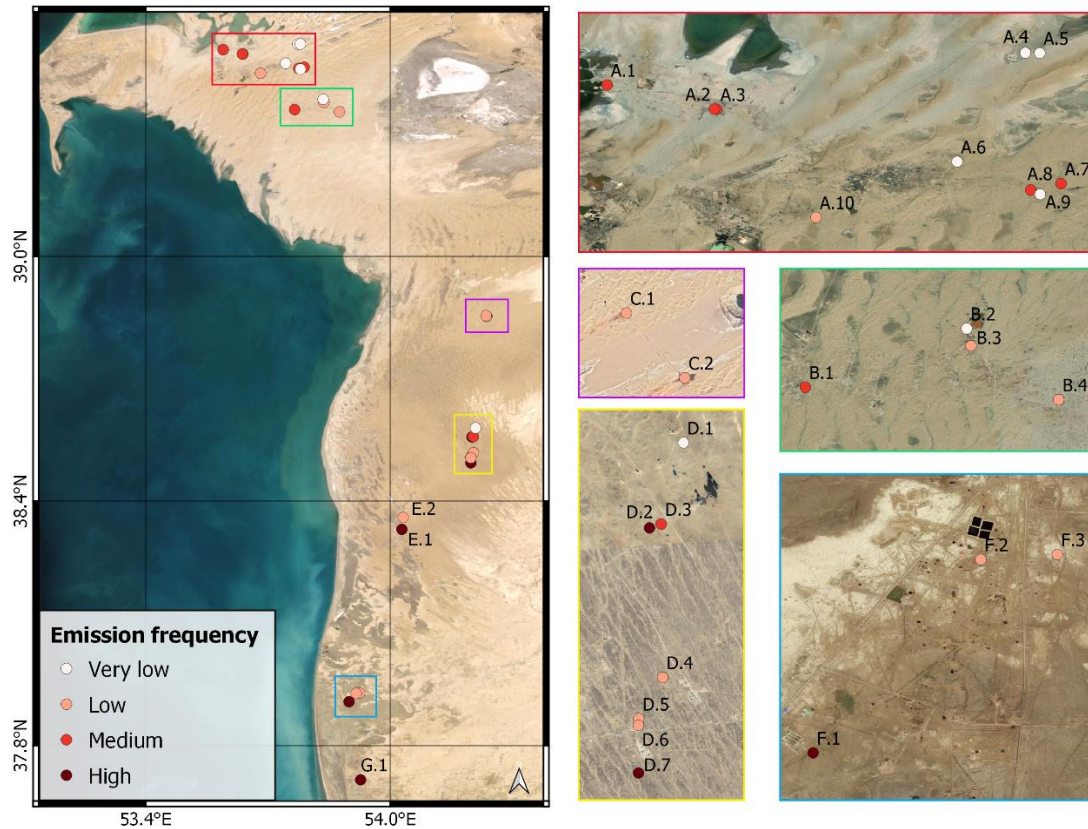
1. M. Etminan, G. Myhre, E. J. Highwood, K. P. Shine, Radiative forcing of carbon dioxide, methane, and nitrous oxide: A significant revision of the methane radiative forcing. *Geophys. Res. Lett.* (2016) <https://doi.org/10.1002/2016GL071930>.
2. M. Saunio, *et al.*, The global methane budget 2000-2017. *Earth Syst. Sci. Data* (2020) <https://doi.org/10.5194/essd-12-1561-2020>.
3. E. G. Nisbet, *et al.*, Very Strong Atmospheric Methane Growth in the 4 Years 2014–2017: Implications for the Paris Agreement. *Global Biogeochem. Cycles* **33**, 318–342 (2019).
4. United Nations Environment Programme and Climate and Clean Air Coalition, “Global Methane Assessment: Benefits and Costs of Mitigating Methane Emissions” (2021).
5. U. N. E. P. (UNEP), Oil and Gas Methane Partnership (OGMP) 2.0 Framework | Climate & Clean Air Coalition. 1–18 (2020).
6. R. A. Alvarez, *et al.*, Assessment of methane emissions from the U.S. oil and gas supply chain. *Science (80-. )*. **361**, 186–188 (2018).
7. D. Zavala-Araiza, *et al.*, Super-emitters in natural gas infrastructure are caused by abnormal process conditions. *Nat. Commun.* **8**, 1–10 (2017).
8. A. R. Brandt, G. A. Heath, D. Cooley, Methane Leaks from Natural Gas Systems Follow Extreme Distributions. *Environ. Sci. Technol.* **50**, 12512–12520 (2016).
9. T. Lauvaux, *et al.*, Global Assessment of Oil and Gas Methane Ultra-Emitters. *ArXiv [Preprint]* (2021) (May 19, 2021).
10. O. S. Ismail, G. E. Umukoro, Global Impact of Gas Flaring. *Energy Power Eng.* **04**, 290–302 (2012).
11. U.S. Department of Energy. Office of Oil and Natural Gas, Natural Gas Flaring and Venting : State and Federal Regulatory Overview , Trends , and Impacts. *U.S. Dep. Energy*, 72 (2019).
12. D. R. Lyon, *et al.*, Aerial Surveys of Elevated Hydrocarbon Emissions from Oil and Gas Production Sites. *Environ. Sci. Technol.* (2016) <https://doi.org/10.1021/acs.est.6b00705>.
13. I. Irakulis-Loitxate, *et al.*, Satellite-based Survey of Extreme Methane Emissions in the Permian Basin. *Sci. Adv.* (2021).
14. A. Gvakharia, *et al.*, Methane, Black Carbon, and Ethane Emissions from Natural Gas Flares in the Bakken Shale, North Dakota. *Environ. Sci. Technol.* **51**, 5317–5325 (2017).
15. D. Zavala-Araiza, *et al.*, A tale of two regions: methane emissions from oil and gas production in offshore/onshore Mexico A tale of two regions: methane emissions from oil and gas production in offshore/onshore Mexico. *Environ. Res. Lett* **16**, 24019 (2021).
16. World Bank Group, Global Gas Flaring Reduction A Public-Private Partnership World Bank Group A VOLUNTARY STANDARD FOR GLOBAL GAS FLARING AND VENTING REDUCTION (2004).
17. EUROPEAN COMMISSION, “COMMUNICATION FROM THE COMMISSION TO THE EUROPEAN PARLIAMENT, THE COUNCIL, THE EUROPEAN ECONOMIC AND SOCIAL COMMITTEE AND THE COMMITTEE OF THE REGIONS on an EU strategy to reduce methane emissions” (2020) (April 14, 2021).
18. IEA, “Methane Tracker 2020” (2020) (May 19, 2021).
19. J. P. Veefkind, *et al.*, TROPOMI on the ESA Sentinel-5 Precursor: A GMES mission for global observations of the atmospheric composition for climate, air quality and ozone layer applications. *Remote Sens. Environ.* **120**, 70–83 (2012).
20. D. H. Cusworth, *et al.*, Detecting high-emitting methane sources in oil/gas fields using satellite observations. *Atmos. Chem. Phys.* **18**, 16885–16896 (2018).
21. Y. Zhang, *et al.*, Quantifying methane emissions from the largest oil-producing basin in the United States from space. *Sci. Adv.* **6**, eaaz5120 (2020).
22. O. Schneising, *et al.*, Remote sensing of methane leakage from natural gas and petroleum systems revisited. *Atmos. Chem. Phys.* **20**, 9169–9182 (2020).
23. J. Barré, *et al.*, Systematic detection of local CH<sub>4</sub> anomalies by combining satellite measurements with high-resolution forecasts. *Atmos. Chem. Phys* **21**, 5117–5136 (2021).

- 618 24. J. A. de Gouw, *et al.*, Daily Satellite Observations of Methane from Oil and Gas Production  
619 Regions in the United States. *Sci. Rep.* **10** (2020).
- 620 25. D. J. Varon, *et al.*, Satellite Discovery of Anomalously Large Methane Point Sources From  
621 Oil/Gas Production. *Geophys. Res. Lett.* **46**, 13507–13516 (2019).
- 622 26. D. H. Cusworth, *et al.*, Multisatellite Imaging of a Gas Well Blowout Enables Quantification  
623 of Total Methane Emissions. *Geophys. Res. Lett.* **48** (2021).
- 624 27. D. J. Varon, *et al.*, High-frequency monitoring of anomalous methane point sources with  
625 multispectral Sentinel-2 satellite observations. *Atmos. Meas. Tech.* **14**, 2771–2785 (2021).
- 626 28. J. D. Maasackers, *et al.*, Space-based identification and quantification of methane  
627 emissions from landfills [in preparation] (2021).
- 628 29. T. Scarpelli, *et al.*, A global gridded (0.1° × 0.1°) inventory of methane emissions from oil,  
629 gas, and coal exploitation based on national reports to the United Nations Framework  
630 Convention on Climate Change. *Earth Syst. Sci. Data Discuss.*, 1–21 (2019).
- 631 30. European Commission Joint Research Centre (EC-JRC), Environmental Assessment  
632 Agency (PBL), Emissions Database for Global Atmospheric Research (EDGAR), release  
633 EDGAR v5.0 (1970 - 2015) of November 2019. Crippa, M., Oreggioni, G., Guizzardi, D.,  
634 Muntean, M., Schaaf, E., Lo Vullo, E., Solazzo, E., Monforti-Ferrario, F., Olivier, J.G.J.,  
635 Vignati, E., Foss. *CO2 GHG Emiss. all world Ctries. - 2019 Report, EUR 29849 EN, Publ.*  
636 *Off.* (2019).
- 637 31. D. Oppo, R. Capozzi, A. Nigarov, P. Esenov, Mud volcanism and fluid geochemistry in the  
638 Cheleken peninsula, western Turkmenistan. *Mar. Pet. Geol.* **57**, 122–134 (2014).
- 639 32. BP, Statistical Review of World Energy, 2020 | 69th Edition. *Bp* **69** (2020).
- 640 33. S. Pirani, *Central Asian Gas: prospects for the 2020* (2019).
- 641 34. *Sustainable Infrastructure for Low-Carbon Development in Central Asia and the Caucasus*  
642 (OECD, 2019) <https://doi.org/10.1787/d1aa6ae9-en> (March 4, 2021).
- 643 35. Rystad Energy - Your Energy Knowledge House (April 18, 2021).
- 644 36. K. Rose, *et al.*, “Development of an Open Global Oil and Gas Infrastructure Inventory and  
645 Geodatabase” (2018) <https://doi.org/10.18141/1427573>.
- 646 37. Torleif Haugland, *et al.*, “Associated petroleum gas flaring study for Russia, Kazakhstan,  
647 Turkmenistan, and Azerbaijan” (2013).
- 648 38. C. Frankenberg, *et al.*, Global column-averaged methane mixing ratios from 2003 to 2009  
649 as derived from SCIAMACHY: Trends and variability. *J. Geophys. Res.* **116**, D04302  
650 (2011).
- 651 39. SkyTruth | Flaring Volume Estimates (March 5, 2021).
- 652 40. R. Calel, P. Mahdavi, The unintended consequences of antiflaring policies—and  
653 measures for mitigation. *Proc. Natl. Acad. Sci. U. S. A.* **117**, 12503–12507 (2020).
- 654 41. C. Frankenberg, *et al.*, Airborne methane remote measurements reveal heavy-tail flux  
655 distribution in Four Corners region <https://doi.org/10.1073/pnas.1605617113> (August 27,  
656 2020).
- 657 42. A. Molod, *et al.*, The GEOS-5 Atmospheric General Circulation Model: Mean Climate and  
658 Development from MERRA to Fortuna. *NASA TM-2012-104606* (2012).
- 659 43. L. Guanter, *et al.*, Mapping methane point emissions with the PRISMA spaceborne  
660 imaging spectrometer arXiv [Preprint] (2021). <https://doi.org/10.31223/X5VC9C> (May 19,  
661 2021)
- 662 44. Sentinel Hub (May 18, 2021).
- 663 45. “S2-PDGS-MPC-DQR” (2021).
- 664 46. Landsat Satellite Missions (June 21, 2021).
- 665 47. C. D. Elvidge, M. Zhizhin, K. Baugh, F. C. Hsu, T. Ghosh, Methods for global survey of  
666 natural gas flaring from visible infrared imaging radiometer suite data. *Energies* **9** (2016).
- 667 48. M. A. Wulder, *et al.*, Current status of Landsat program, science, and applications.  
668 *Remote Sens. Environ.* **225**, 127–147 (2019).
- 669 49. SkyTruth Flaring Map (March 5, 2021).
- 670

671 **Figures and Tables**



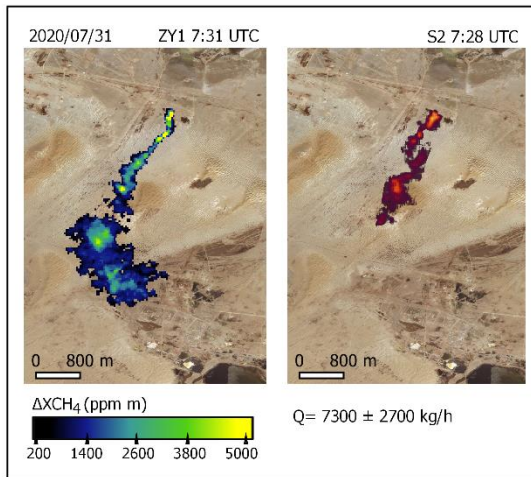
672  
 673 **Figure 1.** Representation of the study area. Left, oil and gas fields classified according to the type  
 674 of production activity based on Rystad database (35): oil, gas, condensate, liquefied natural gas  
 675 (LNG), and the combination of several of them; the location of processing plants, terminals,  
 676 compressor stations and pipelines along the South Caspian Basin as provided in (36) are also  
 677 depicted. Right, 0.1° composite of CH<sub>4</sub> concentration in the atmospheric column from TROPOMI  
 678 data between November 2018 and November 2020. Background satellite image from ESRI.  
 679  
 680



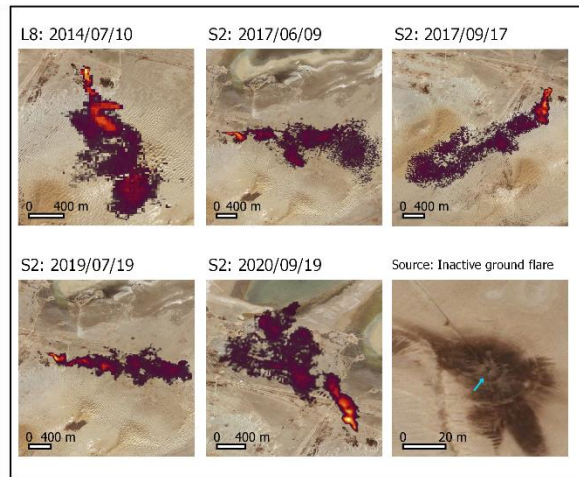
681  
 682  
 683  
 684  
 685  
 686  
 687  
 688  
 689  
 690  
 691

**Figure 2.** Spatial distribution of point emissions in Turkmenistan’s South Caspian Basin. The emission frequency corresponds to the number of emissions detected by S2 with respect to the number of clear-sky days with S2 overpasses between 2017 and 2020, where “high” represents an emission frequency range between 48 - 37 %, “medium” 37 - 15 %, “low” 15 - 3 %, and “very low” 3 - 1 %. Emission points are labeled with alphanumeric codes. Codes with the same letter belong to the same field. Background images are extracted from the most recent high-resolution imagery in the ESRI, Google Satellite or Bing Aerial web portals.

## Detection &amp; quantification

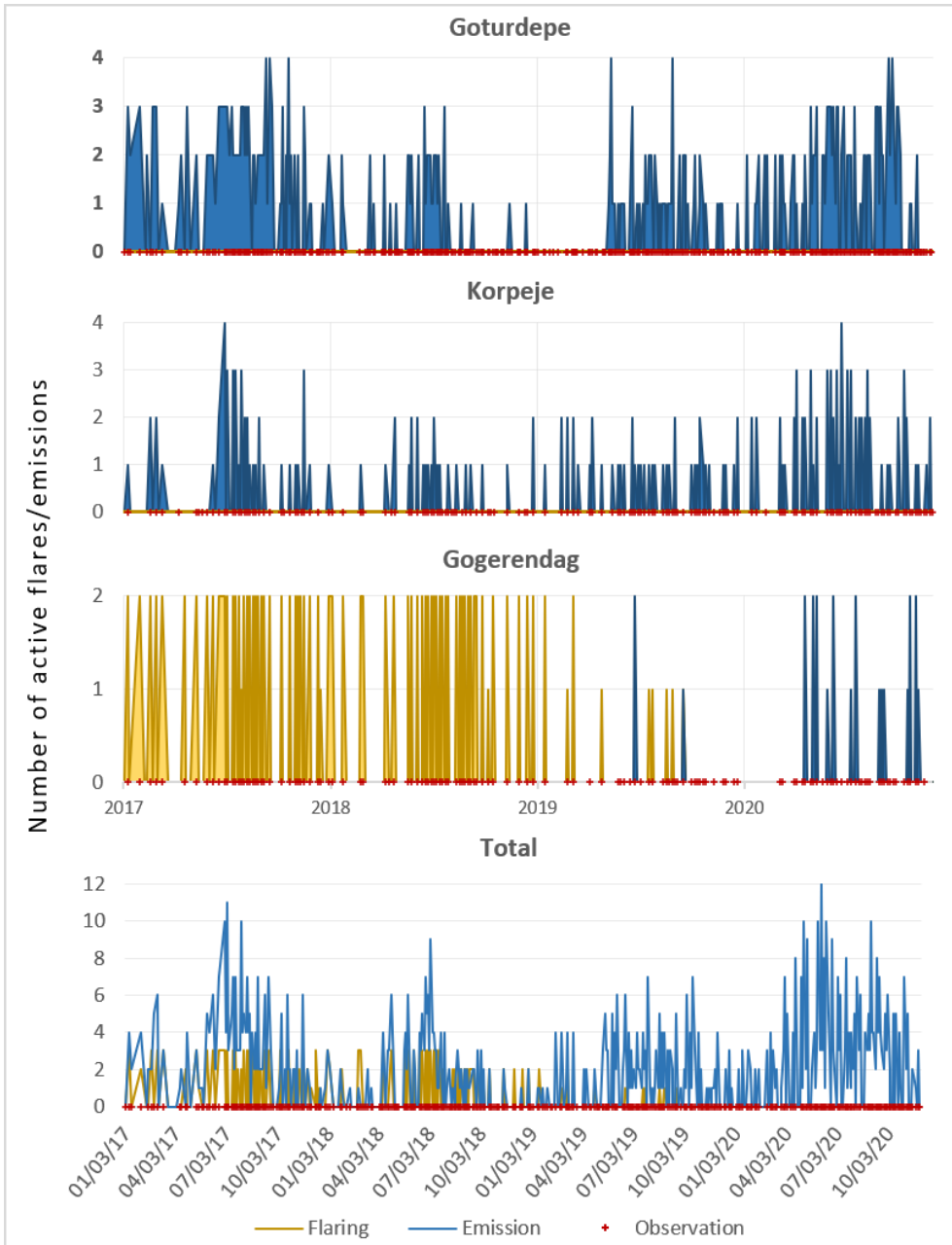


## Monitoring &amp; attribution



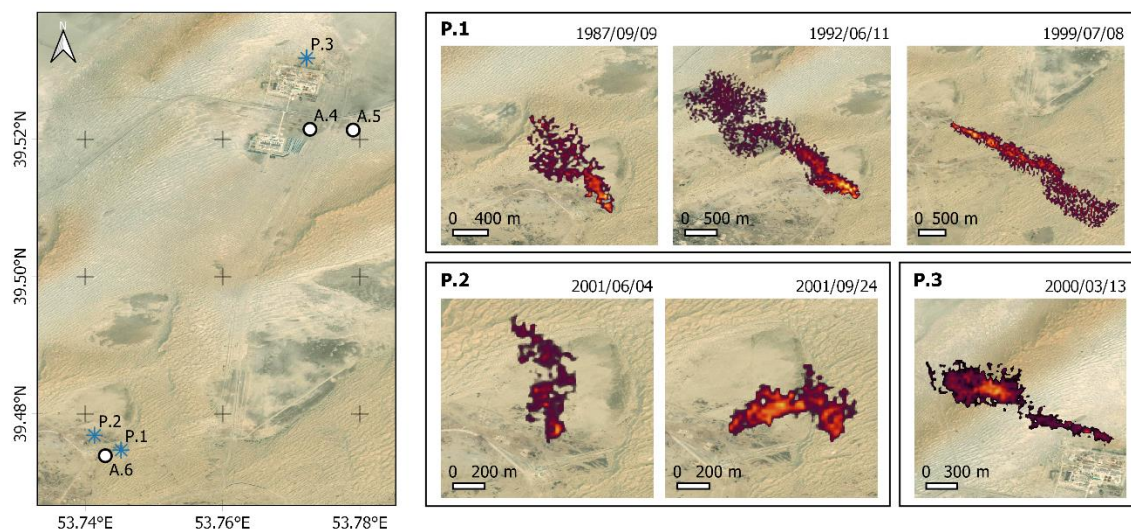
693  
694  
695  
696  
697  
698  
699  
700

**Figure 3.** Examples of emissions detected from the A.3 emission point (see Fig. 2). Left, plume detected by both ZY1 and S2 within a 3-minute time difference. Right, time series of plumes detected at A.3 with the S2 and L8 multispectral satellites. A true-color composite of the emission point, based on visual imagery, is shown in the lower right corner. The background image for all panels is from Bing Aerial.



701  
 702  
 703  
 704  
 705  
 706  
 707  
 708

**Figure 4.** Temporal evolution of emissions in the Goturdepe (A.X), Korpeje (D.X) and Gogerendag (C.X) fields, as well as the daily total number of active emissions detected from the 29 sites found in this study. The vertical axis indicates the number of points that were emitting or flaring at the same time on the same day.



709

710 **Figure 5.** Examples of plume detections in the Goturdepe field using historical data from the L5  
 711 multispectral satellite mission. On the left, the general map showing the location of P.1, P.2 and  
 712 P.3 emitters, which were active during the L5 monitoring period, and the nearby emitters (A.4,  
 713 A.5, and A.6) active during the S2 monitoring period. On the right, some of the detected plumes  
 714 from P.1, P.2 and P.3. The background image of all panels is from ESRI Satellite.

715 **Table 1.** Classification of oil and gas production fields where emissions have been found. "Field"  
 716 refers to the name of the field; "Oil and Gas Category" is the type of production activity in each field;  
 717 "Production" is the amount of production in kbbl/day in the years 2018-2020; "Number of emitters"  
 718 is the number of emitting points that have been found in each field; "Detected emissions" is the  
 719 number of days with emissions that have been observed by year; and "Total emissions" is the total  
 720 number of plumes observed in each field in the entire study period. Oil and Gas category and  
 721 production data is based on Rystad database (35).

Field	Oil and Gas Category	Production (kbbl/d)			Number of emitters	Detected emissions				Total emissions
		2018	2019	2020		2017	2018	2019	2020	
Goturdepe	Crude Oil	43.014	30.000	30.137	10	138	50	64	141	393
	Condensate	0.001	0.001	0.001						
	NGL	0.060	0.042	0.042						
Barsa-Gelmez	Crude Oil	28.000	20.000	13.667	4	32	39	23	32	126
	Condensate	0.001	0.001	0.059						
	NGL	0.021	0.015	0.029						
Gogerendag	Crude Oil	0.000	0.000	0.007	2	0	0	3	21	24
	Condensate	0.003	0.004	0.009						
Korpeje	Crude Oil	0.003	0.003	0.046	7	45	25	43	74	187
	Condensate	0.002	0.002	0.002						
	NGL	0.160	0.160	0.158						
	Gas	18.919	18.919	18.879						
Gamysljja Gunorta	Crude Oil	0.004	0.003	0.768	2	7	14	24	28	73
	Condensate	0.003	0.003	0.683						
Keymir	Crude Oil	0.003	0.004	4.648	3	7	17	25	41	90
	Condensate	0.001	0.001	4.212						
	NGL	0.028	0.028	0.650						
Akpatlavuk	Crude Oil	0.004	0.003	0.000	1	21	16	12	2	51
	Condensate	0.003	0.003	0.000						
<b>Total</b>		90.23	69.19	74.00	28	250	161	194	339	944

722

723

724 **Supplementary Information for**

725 Satellites unveil easily-fixable super-emissions in one of the world's  
726 largest methane hotspot regions

727

728 Itziar Irakulis-Loitxate<sup>1\*</sup>, Luis Guanter<sup>1</sup>, Joannes D. Maasakkers<sup>2</sup>, Daniel Zavala-Araiza<sup>3,4</sup>, Ilse  
729 Aben<sup>2</sup>

730

731 \* Correspondence to: iiraloi@doctor.upv.es

732

733

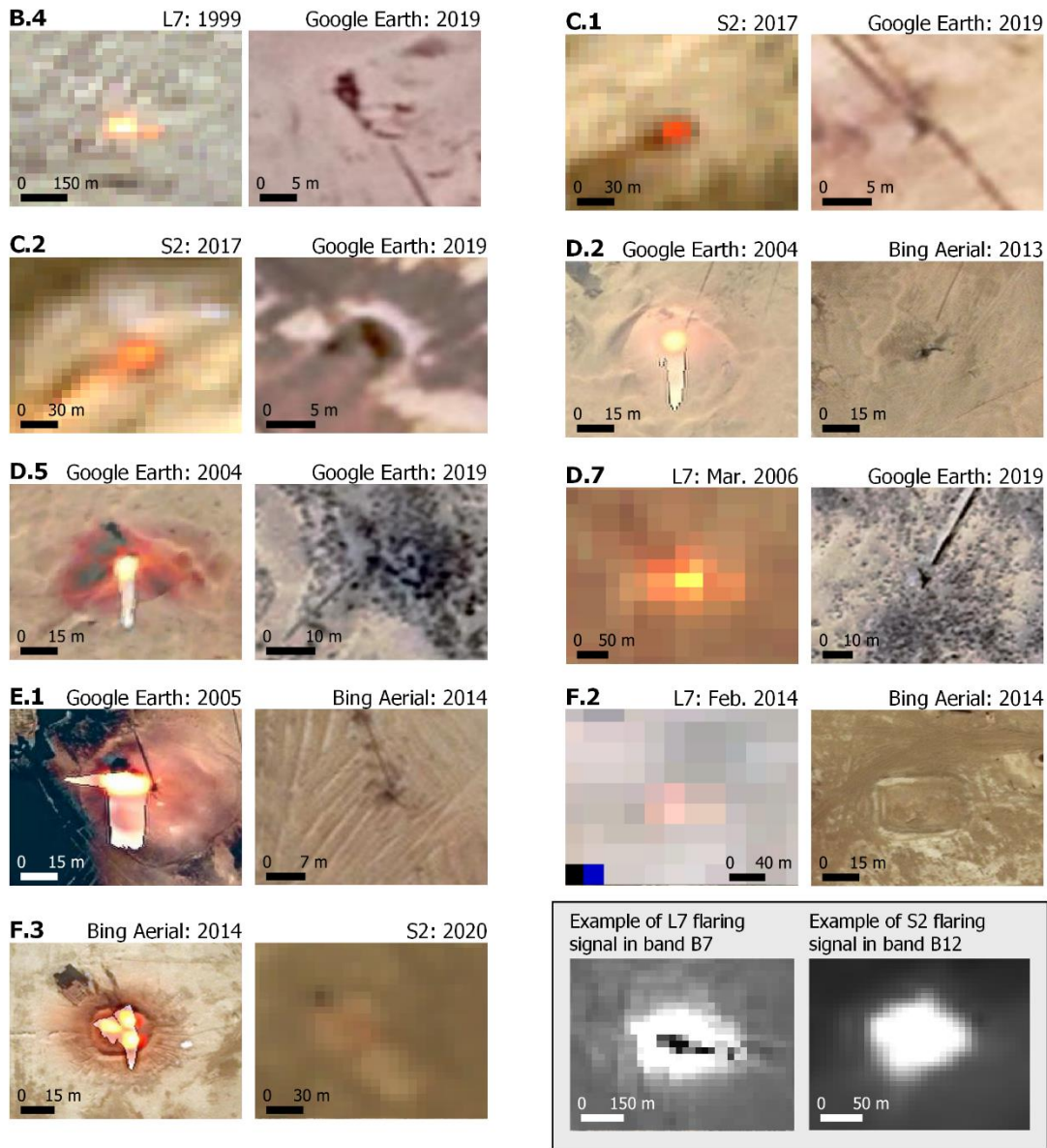
734 **This section includes:**

735

736           Figures S1 to S11

737           Tables S1 to S1

738           SI References

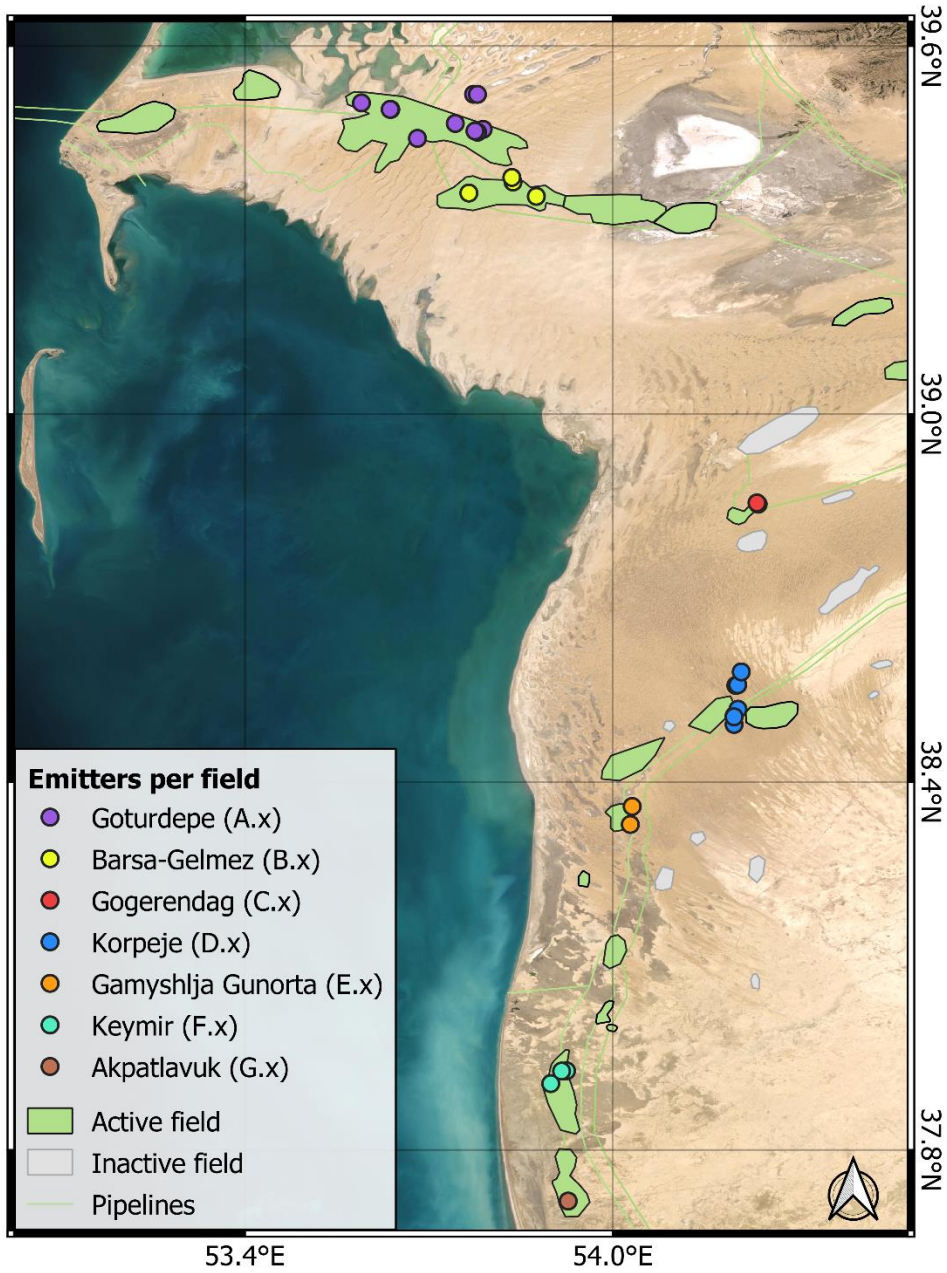


739

740 **Fig. S1.** Flares with active flaring in the past and current inactive appearance seen in RGB. Bottom  
 741 right two examples of active flares as seen in the Landsat 7 (L7) B7 and S2 B12 bands (points D.7  
 742 and C.2 respectively), i.e. in the CH<sub>4</sub> absorption bands. In the Landsat B7 and S2 B12 bands, the  
 743 CH<sub>4</sub> absorbs the signal (low values), while the flaring emits a very high signal (very high values)  
 744 compared to the surface.

745

746

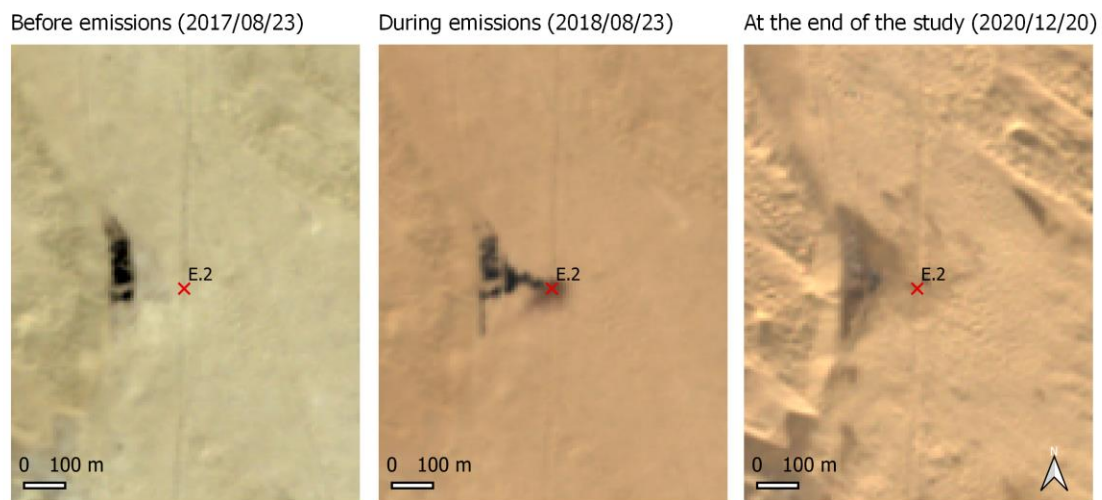


747

748 **Fig. S2.** Distribution of the detected points according to the field they belong to. The area of the  
 749 fields is based on the data from Rose et al. 2018 (36). The extension of some fields has been  
 750 manually updated due to their expansion in recent years.

751

752

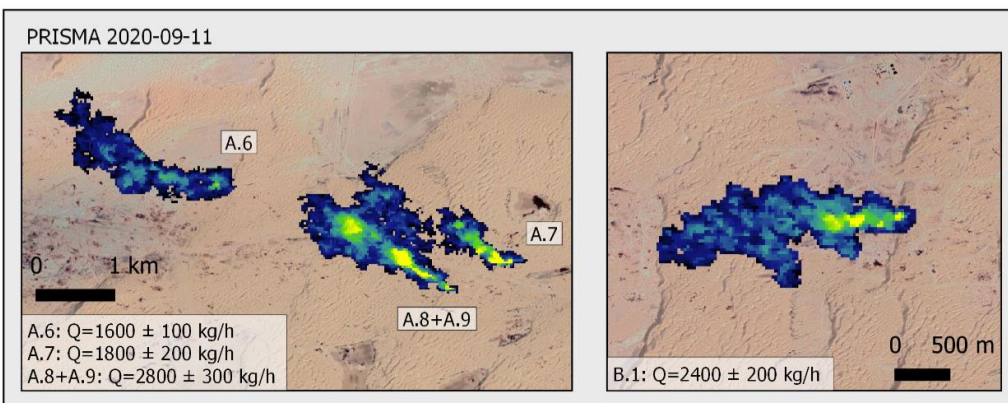
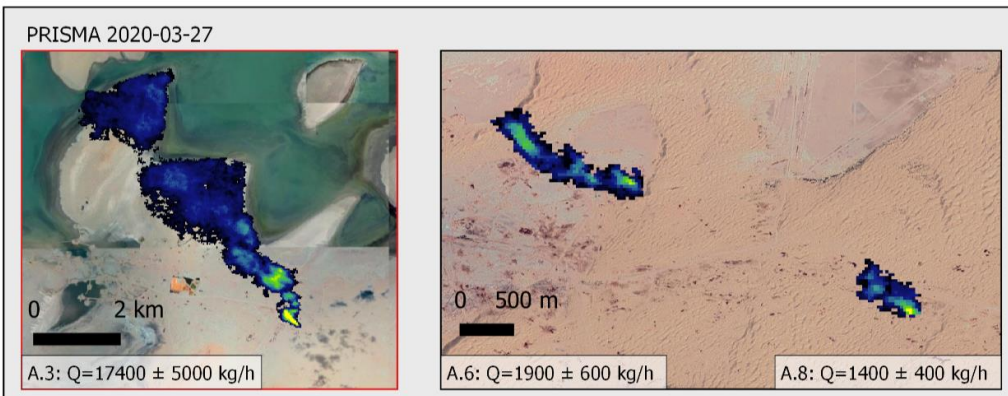
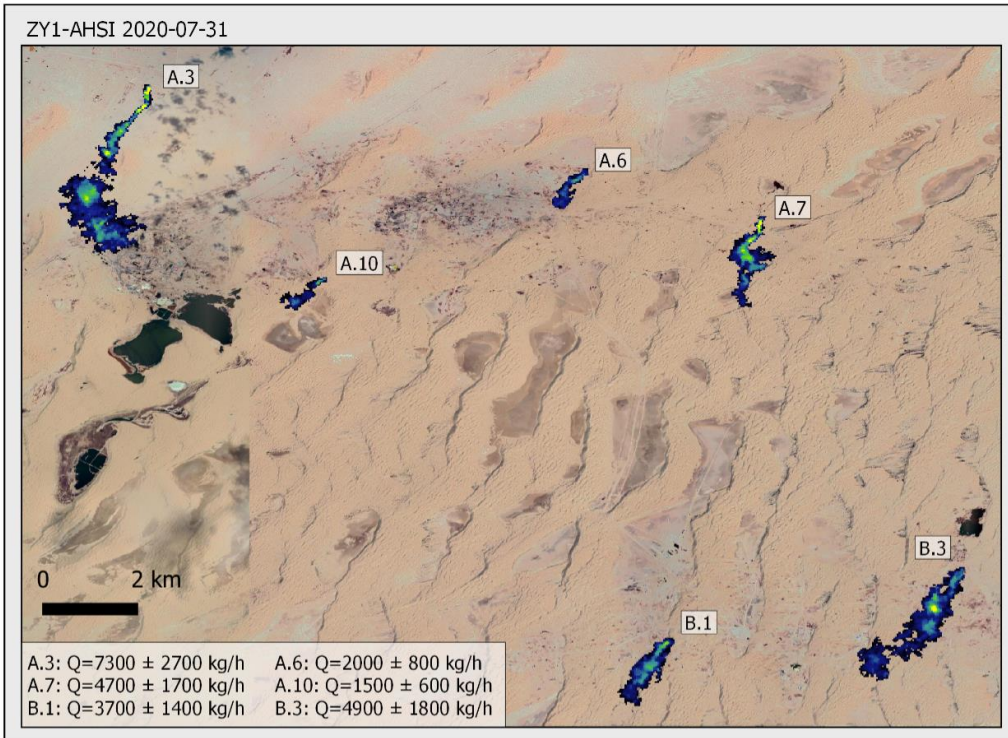


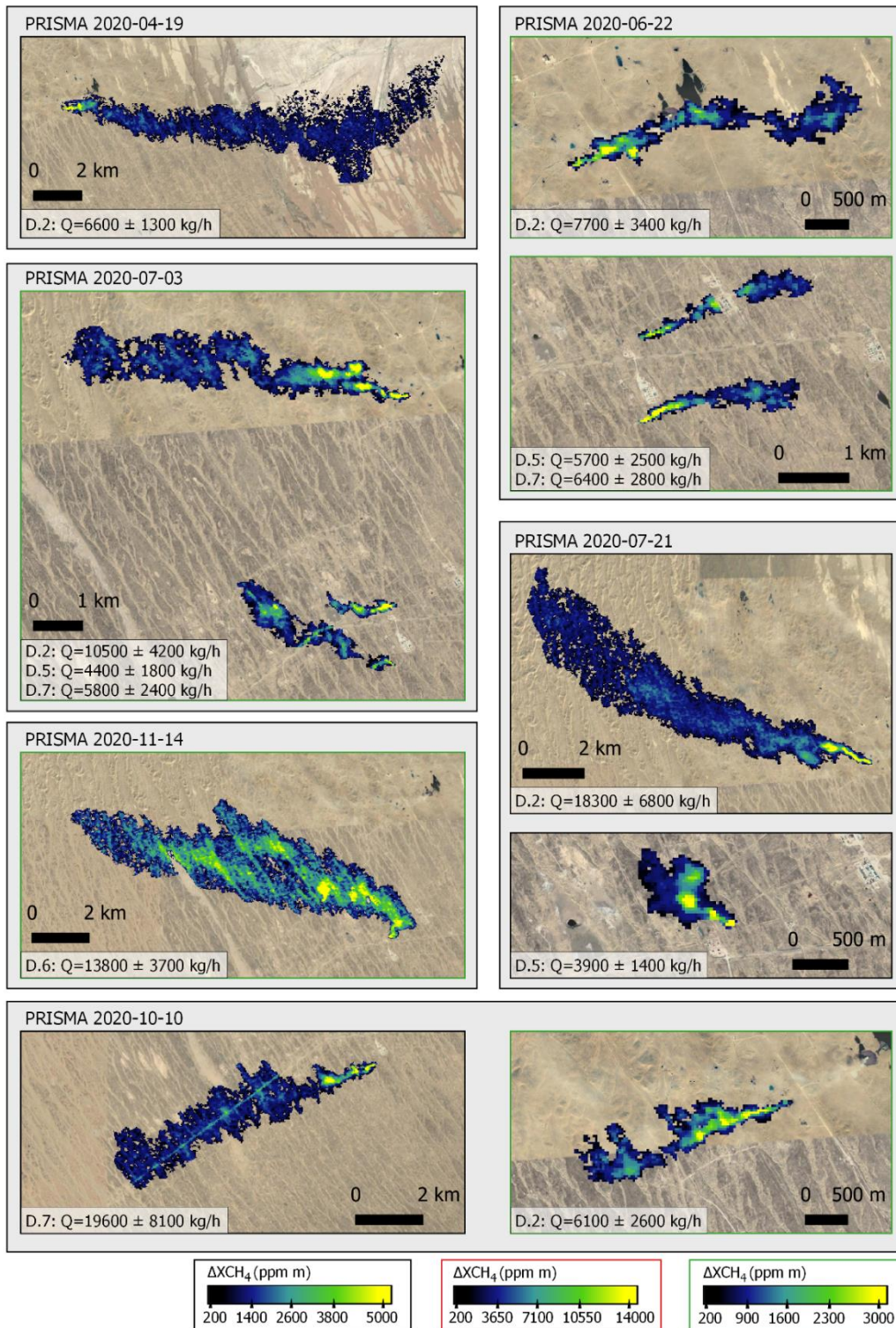
753

754 **Fig. S3.** The evolution of the E.2 emission point seen in RGB before, during and after the emissions  
755 derived from a leak. During the emission period a black liquid emanating from the emission point  
756 is visible.

757

758

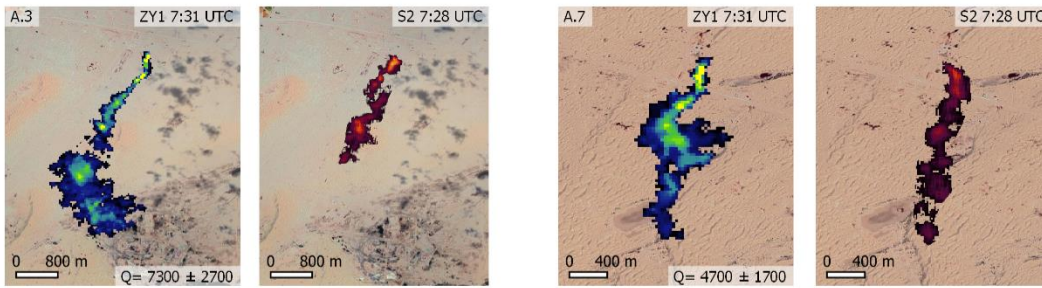




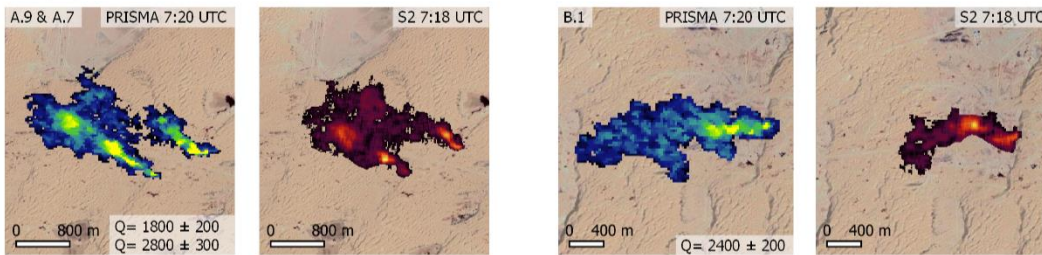
760

761 **Fig. S4.** All CH<sub>4</sub> plumes detected with the ZY1 and PRISMA hyperspectral satellites in the survey  
 762 period. The color scale corresponding to each plume is indicated with the color of the map outline  
 763 (black, red, or green).

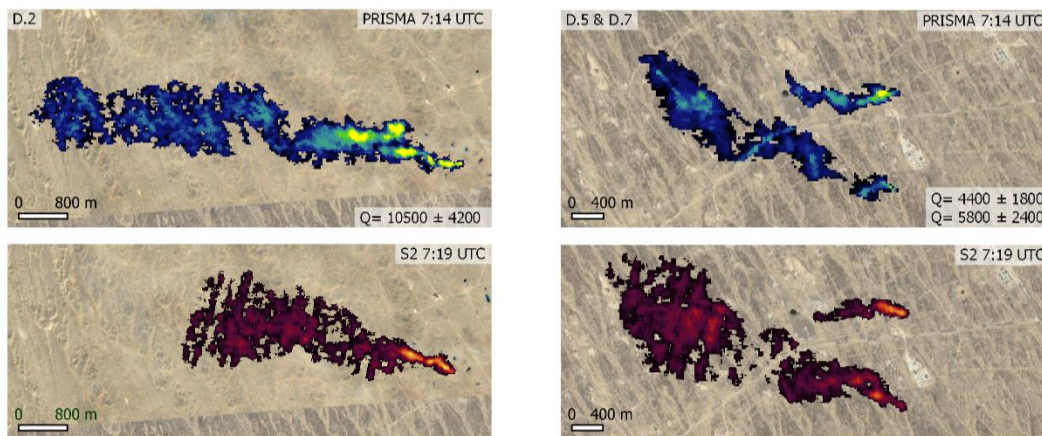
2020/07/31



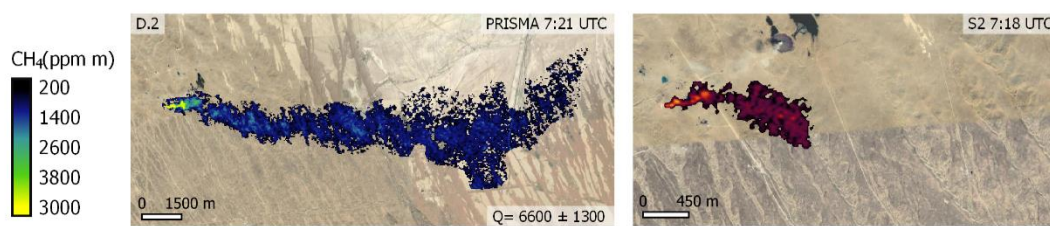
2020/09/11



2020/07/03



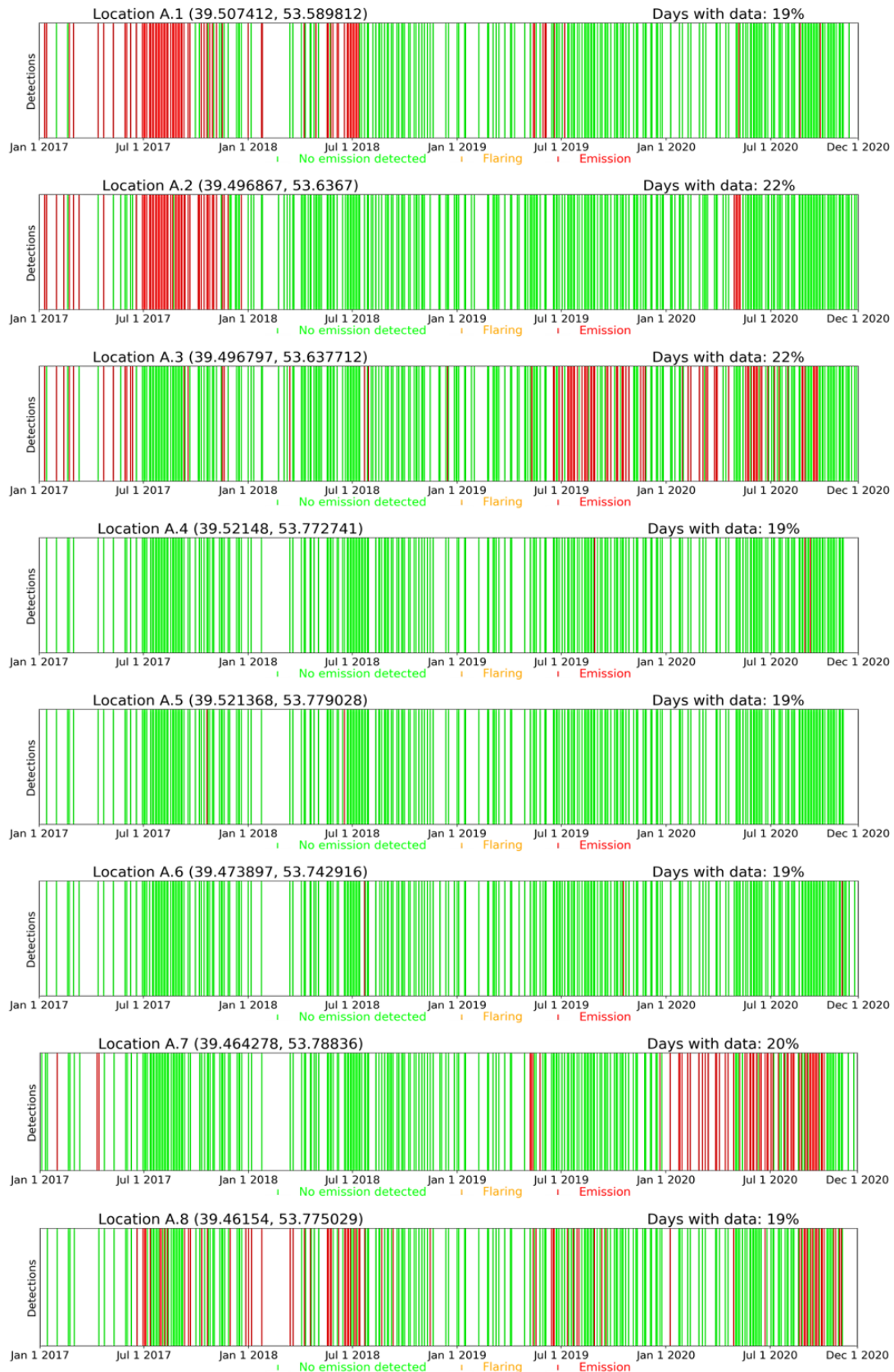
2020/04/19

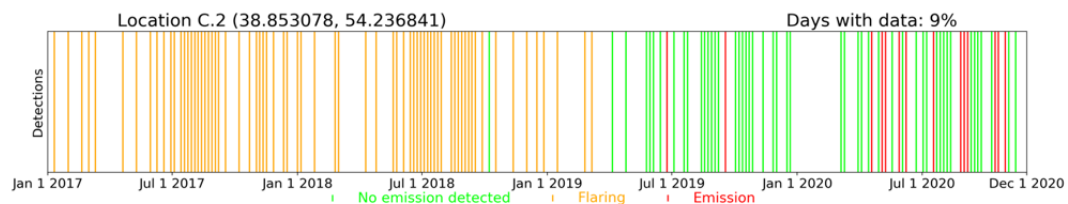
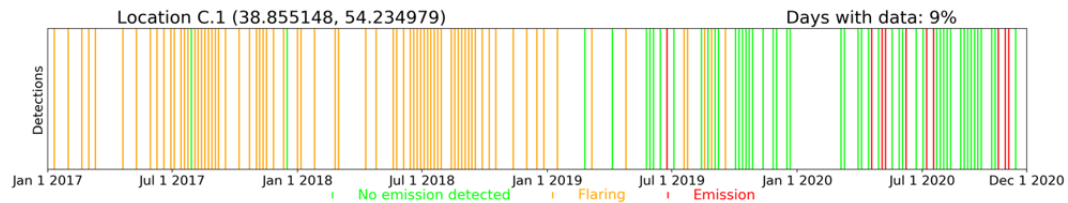
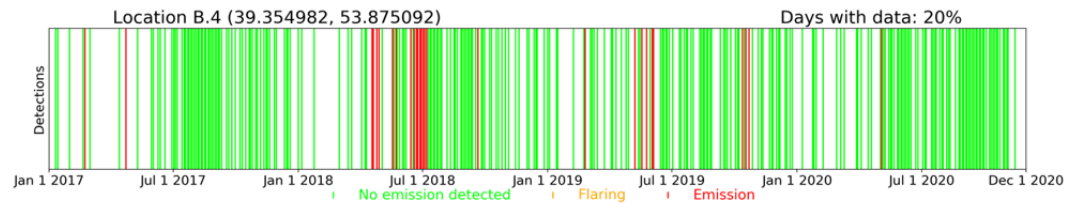
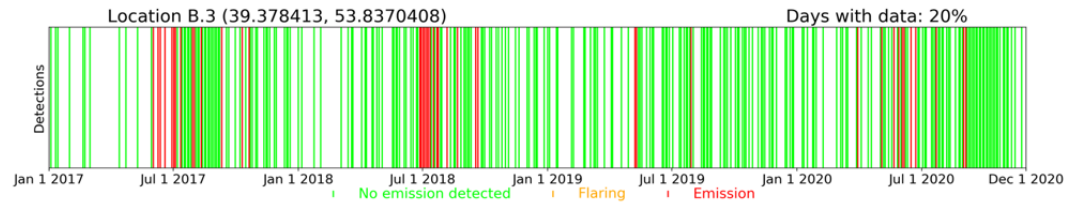
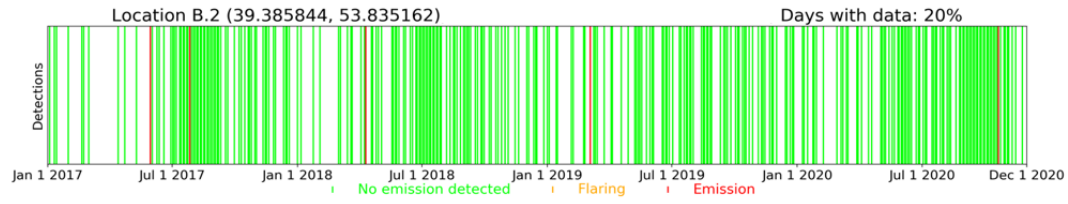
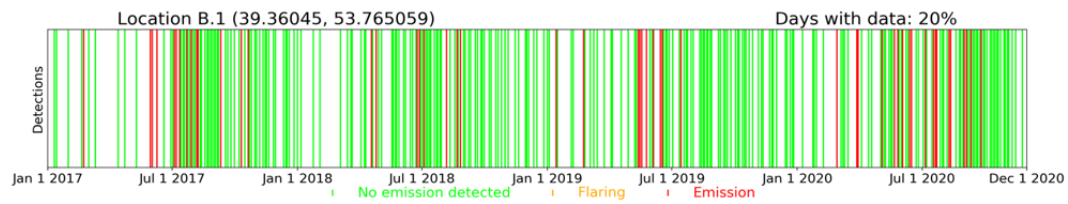
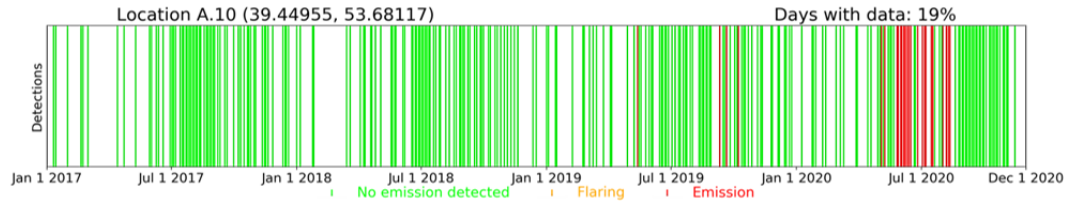
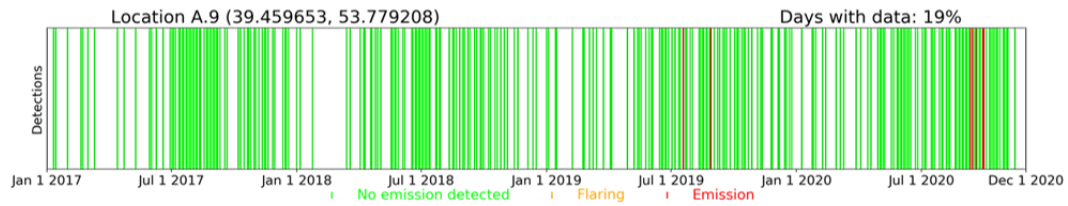


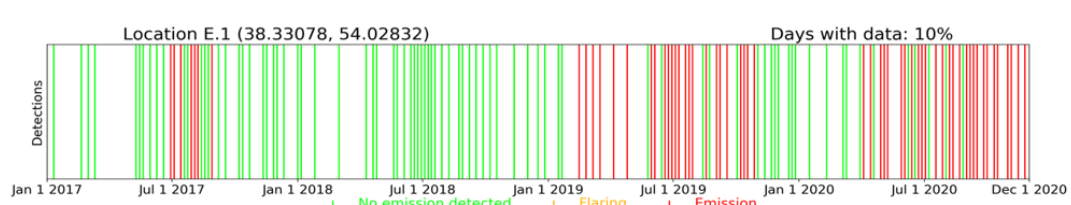
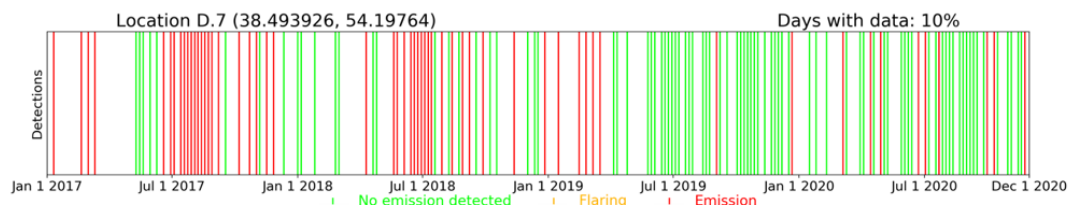
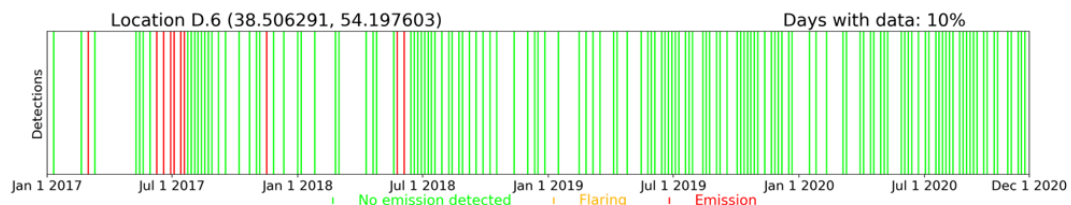
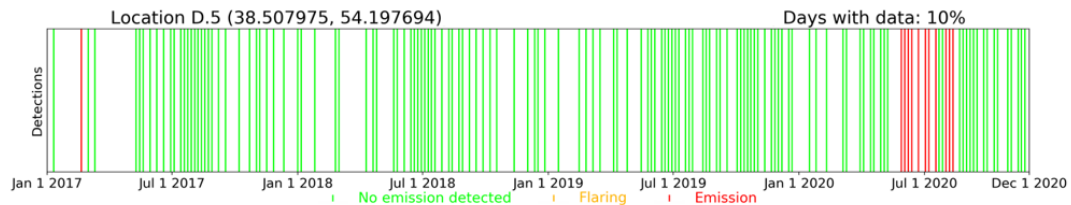
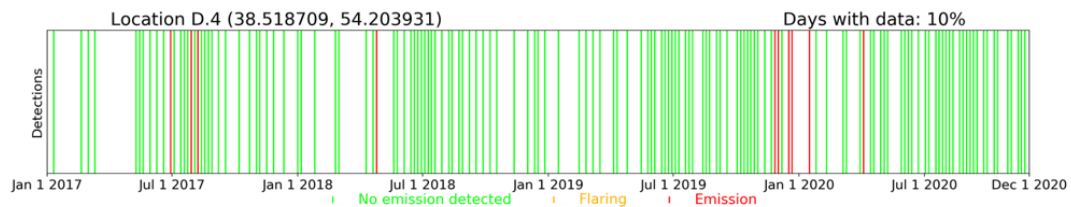
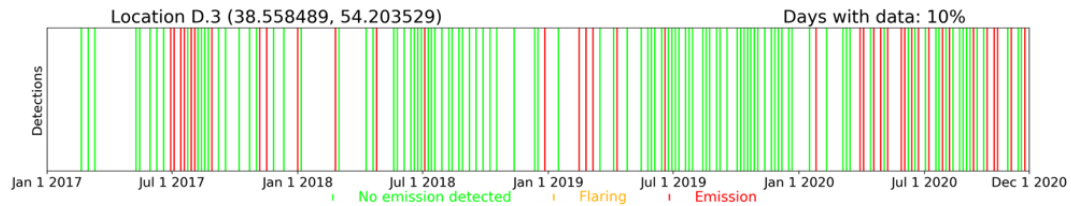
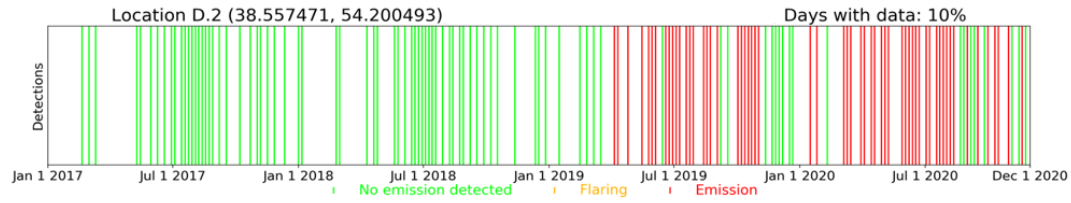
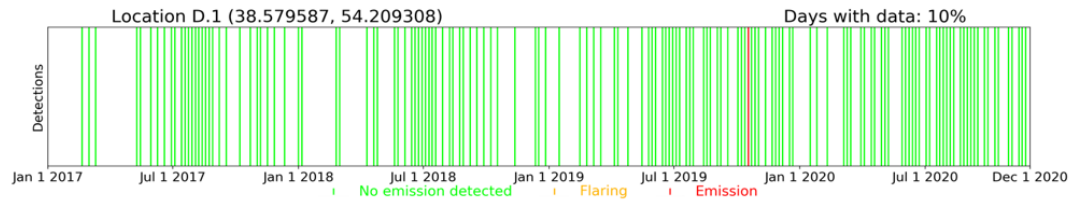
764

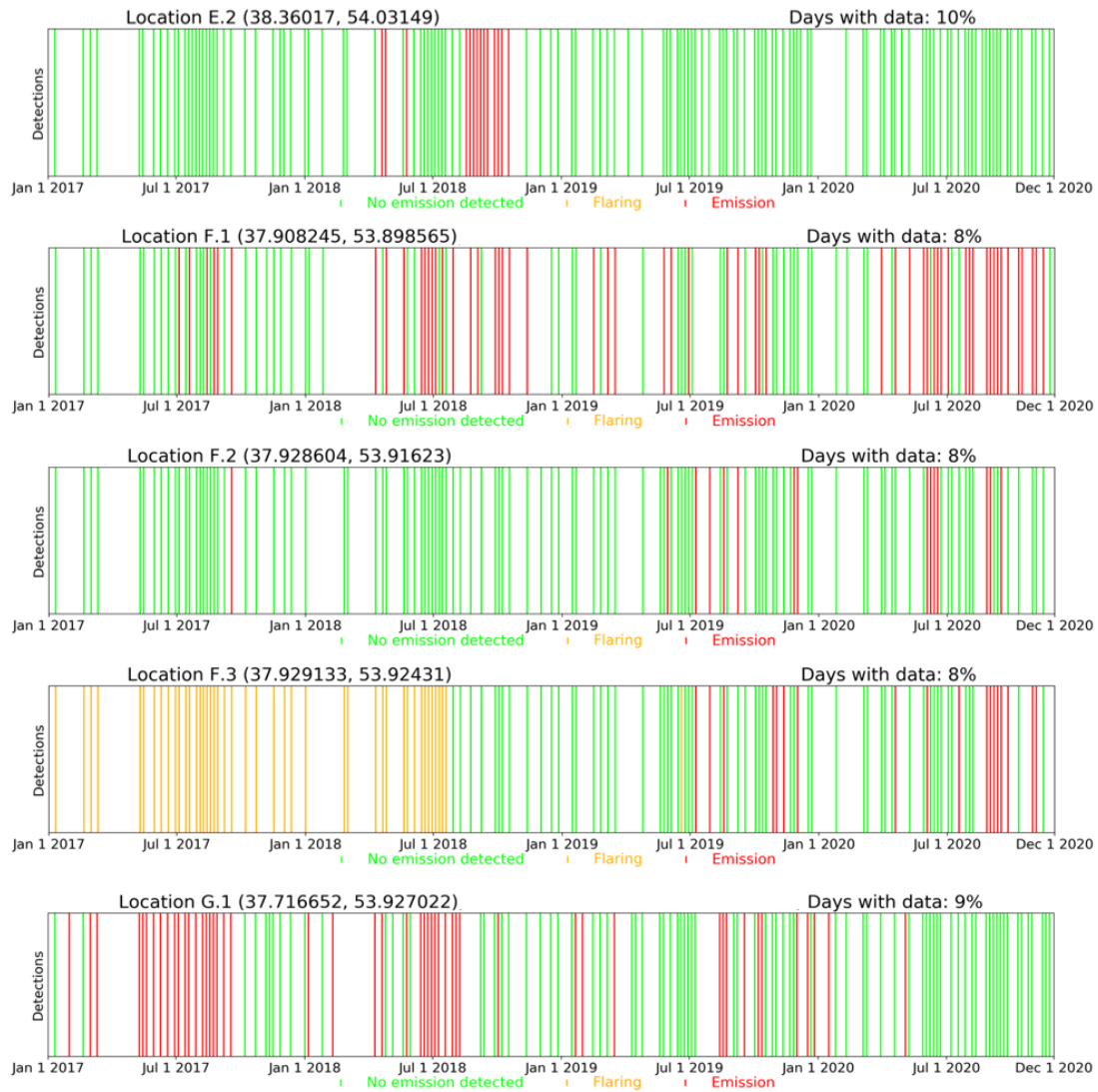
765 **Fig. S5.** Simultaneous detections of Sentinel 2 (S2) CH<sub>4</sub> plumes with PRISMA and ZY1 satellites  
766 within minutes of each other.

767





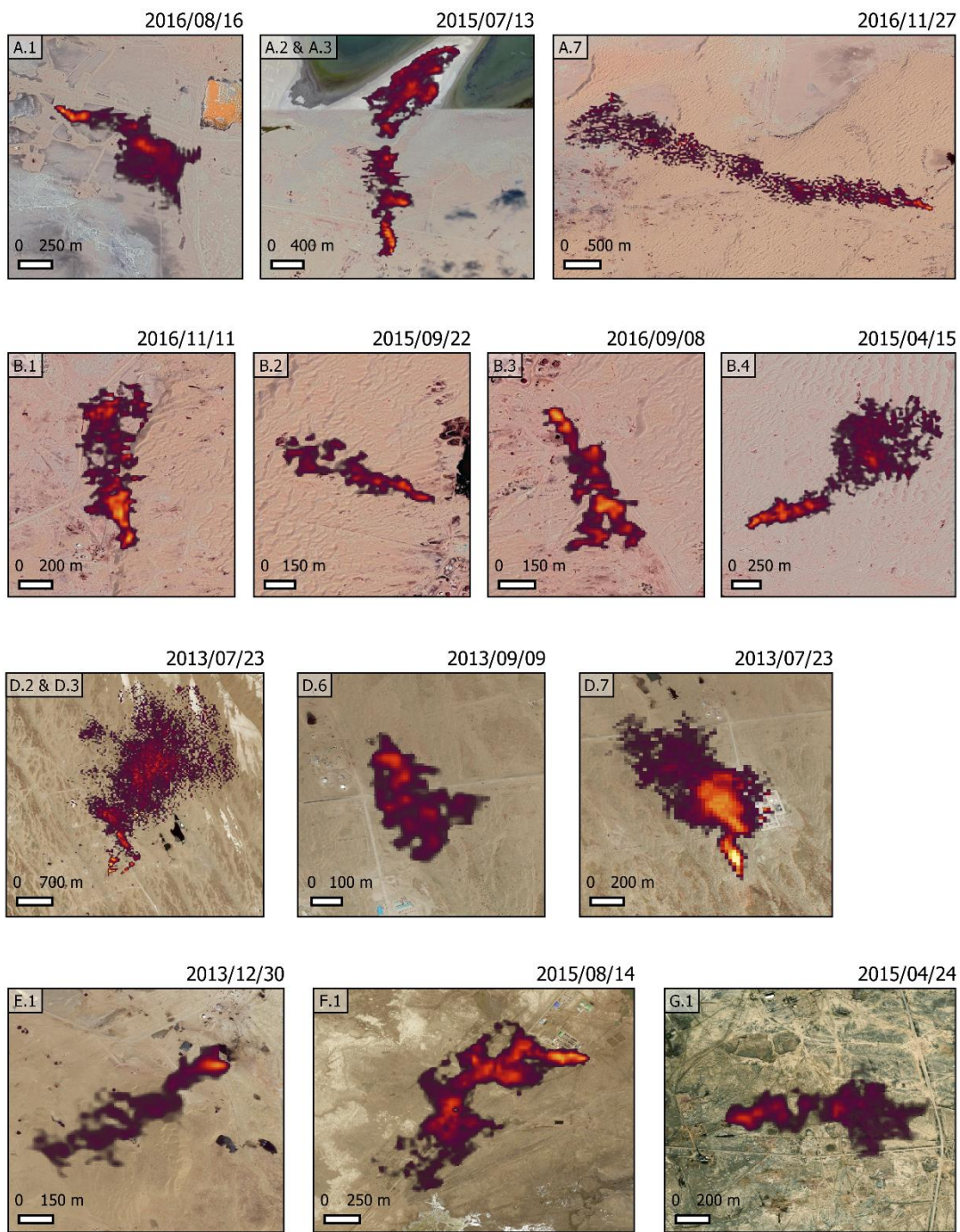




771

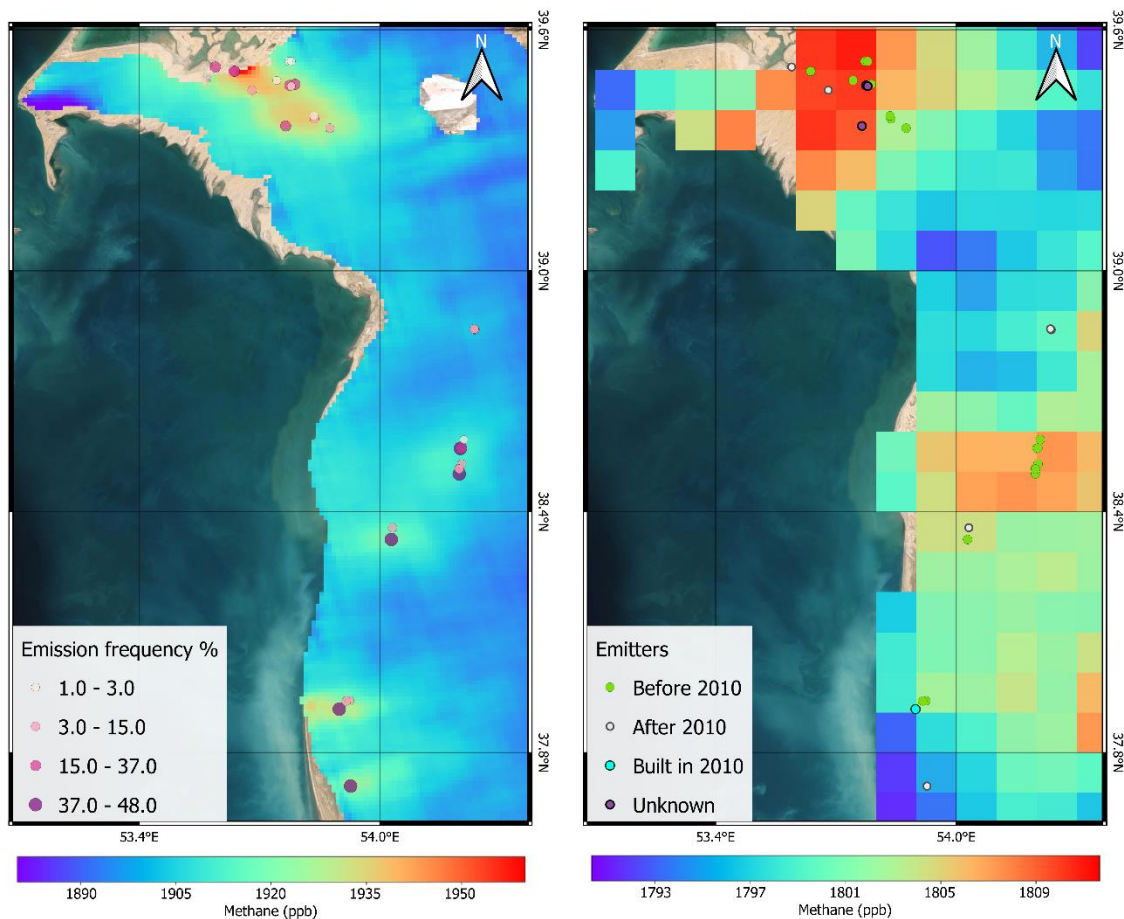
772 **Fig. S6.** The temporal evolution of the 29 emitters identified during 2017-2020 with S2, where  
 773 green lines indicate no emission day, red lines indicate emission, and yellow lines indicate active  
 774 flaring. Cloudy sky days are not included in the series. The Goturdepe (A.X) and Barsa-Gelmez  
 775 (B.X) emitters contain double data days because two S2 orbits overlap in that area.

776



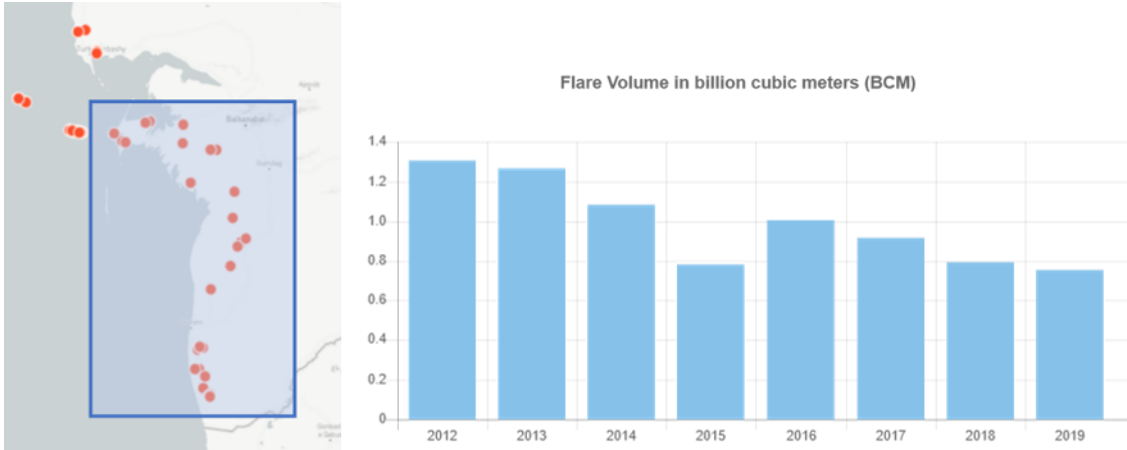
777

778 **Fig. S7.** Some Landsat 8 detections from sources that record emissions prior to Sentinel 2  
 779 monitoring period.



780  
 781  
 782  
 783  
 784  
 785  
 786  
 787  
 788  
 789  
  
 790  
 791

**Fig. S8.** Combination of moderate and low-resolution data from TROPOMI and SCIAMACHY sensors respectively with the emitter points indicated. On the left, the oversampled TROPOMI data between 2018 and 2020 combined with the emitters represented in terms of emission frequency. On the right the SCIAMACHY data oversampled to a  $0.1^\circ \times 0.1^\circ$  grid between 2003 and 2010 combined with the emitters found in this study classified according to their possible contribution to the SCIAMACHY data, i.e., whether the emitter existed before 2010 (it could have contributed to the  $\text{CH}_4$  enhancement), post-2010 (it could not have contributed), undefined (unidentified emitters) or if it was constructed just in 2010 (it existed in the SCIAMACHY observation period but its contribution should be minimal).

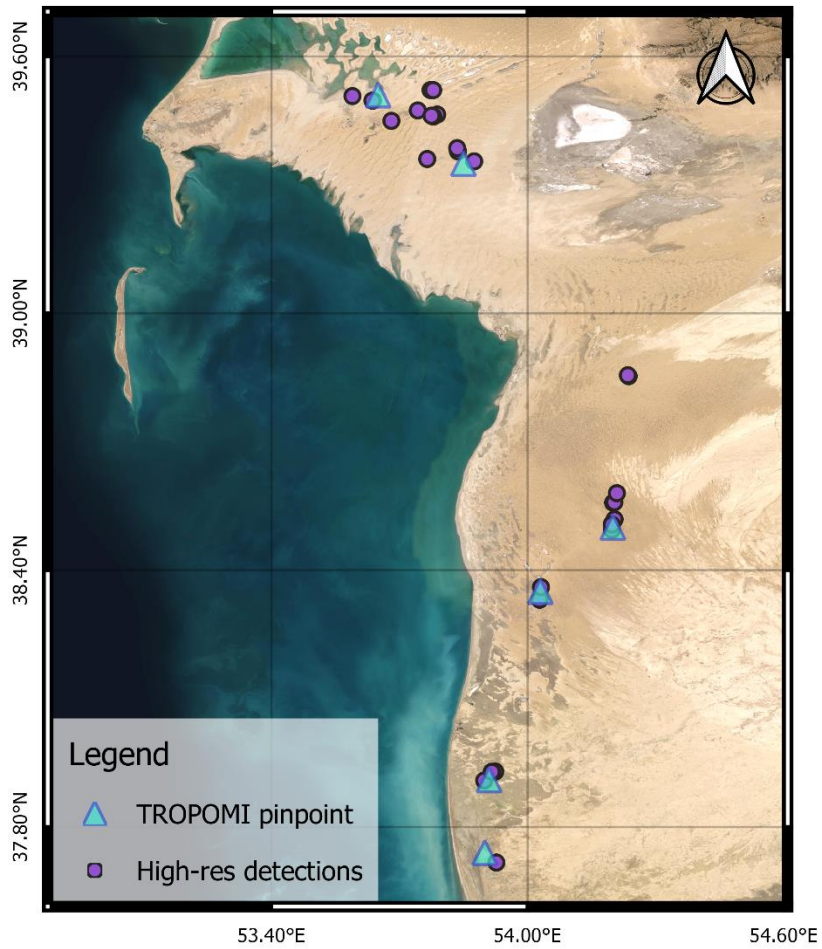


792

793 **Fig. S9.** VIIRS detected flaring over the years. On the left, inside the blue box, the onshore area of  
 794 the South Caspian Basin that has been studied in this work, with the points where VIIRS detected  
 795 flaring between 2012 and 2019. On the right the flared gas volume in that area according to VIIRS  
 796 records each year (47). These data have been obtained from SkyTruth's Annual Flare Volume map  
 797 (39).

798

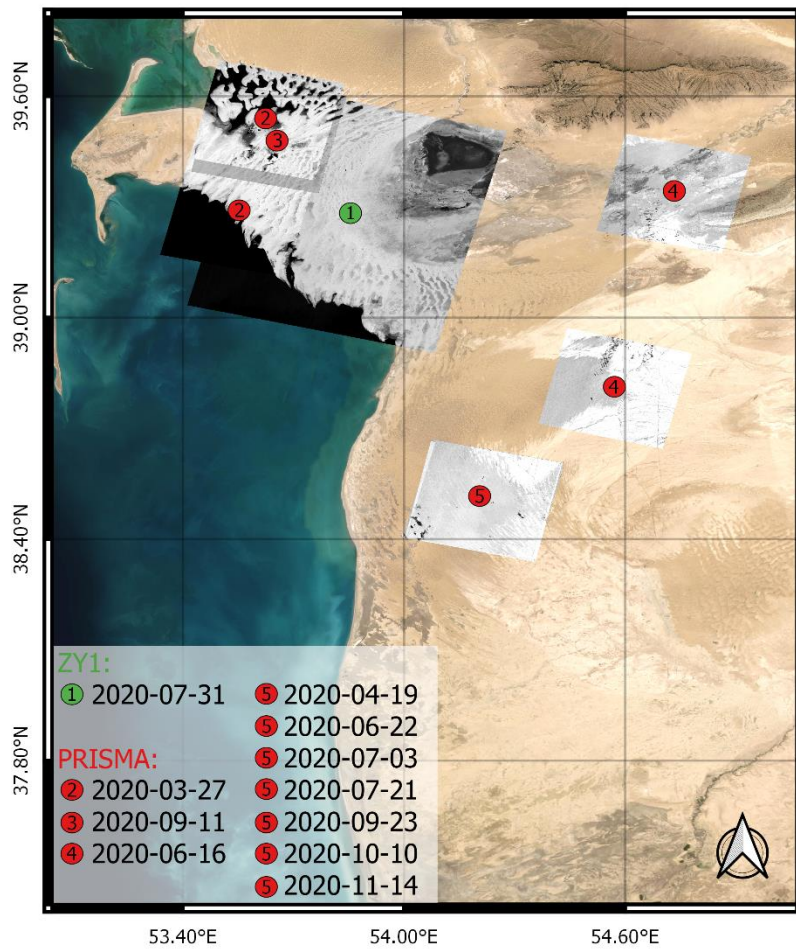
799



800

801 **Fig. S10.** The locations pinpointed by TROPOMI (blue triangles), and the emitter points (purple  
 802 circles) found in the study.

803



804

805 **Fig. S11.** Spatial coverage of ZY1 and PRISMA hyperspectral data used in this work.

806

807 **Table S1.** Emissions point list. Where "Point ID" is the identifying name assigned to this study. Lat  
 808 and Long coordinates of the emitter. "Emitter" the type of emitter or source. "O. E. %" is Observed  
 809 emission %, that is, the percentage of clear-sky days with emissions above the detection limit of  
 810 S2, and this data is used throughout the document to refer to the emission frequency. "Field" field  
 811 where it is located.

Point ID	Lat	Long	Emitter	O.E.%	Field
A.1	39.50741	53.58981	Ground flare	29	Goturdepe
A.2	39.49687	53.6367	Ground flare	20	Goturdepe
A.3	39.4968	53.63771	Ground flare	29	Goturdepe
A.4	39.52148	53.77274	Pit flare	1	Goturdepe
A.5	39.52137	53.77903	Ground flare	1	Goturdepe
A.6	39.4739	53.74292	Ground flare	1	Goturdepe
A.7	39.46428	53.78836	Pit flare	21	Goturdepe
A.8	39.4616	53.77502	Undefined	27	Goturdepe
A.9	39.45965	53.77921	Undefined	3	Goturdepe
A.10	39.44955	53.68117	Pipeline	9	Goturdepe
B.1	39.36045	53.76506	Undefined	18	Barsa-Gelmez
B.2	39.38584	53.83516	Ground flare	2	Barsa-Gelmez
B.3	39.37841	53.83704	Ground flare	14	Barsa-Gelmez
B.4	39.35498	53.87509	Ground flare	10	Barsa-Gelmez
C.1	38.85515	54.23498	Ground flare	7	Gogerendag
C.2	38.85308	54.23684	Ground flare	10	Gogerendag
D.1	38.57959	54.20931	Ground flare	1	Korpeje
D.2	38.55747	54.20049	Ground flare	41	Korpeje
D.3	38.55849	54.20353	Pit flare	26	Korpeje
D.4	38.51871	54.20393	Ground flare	7	Korpeje
D.5	38.50798	54.19769	Ground flare	8	Korpeje
D.6	38.50629	54.1976	Ground flare	7	Korpeje
D.7	38.49393	54.19764	Ground flare	39	Korpeje
E.1	38.33078	54.02832	Ground flare	42	Gamyshlja Gunorta
E.2	38.36017	54.03149	Pipeline	10	Gamyshlja Gunorta
F.1	37.90825	53.89857	Elevated flare	48	Keymir
F.2	37.9286	53.91623	Pit flare	12	Keymir
F.3	37.92913	53.92431	Pit flare	15	Keymir
G.1	37.71665	53.92702	Pit flare	38	Akpatlavuk

812  
 813

814 **SI References**

815

816 1. K. Rose, *et al.*, "Development of an Open Global Oil and Gas Infrastructure Inventory and  
817 Geodatabase" (2018) <https://doi.org/10.18141/1427573>.

818 2. C. D. Elvidge, M. Zhizhin, K. Baugh, F. C. Hsu, T. Ghosh, Methods for global survey of  
819 natural gas flaring from visible infrared imaging radiometer suite data. *Energies* **9** (2016).

820 3. SkyTruth | Flaring Volume Estimates (March 5, 2021).

821